

TIME AND SPACE-RESOLVED ENERGY FLUX MEASUREMENTS IN  
THE DIVERTOR OF THE ASDEX TOKAMAK BY COMPUTERIZED  
INFRARED THERMOGRAPHY

E.R. Müller, B.K. Bein<sup>+</sup>, K. Steinmetz

IPP III/97

June 1984



**MAX-PLANCK-INSTITUT FÜR PLASMAPHYSIK**

**8046 GARCHING BEI MÜNCHEN**



# MAX-PLANCK-INSTITUT FÜR PLASMAPHYSIK

## GARCHING BEI MÜNCHEN

TIME AND SPACE-RESOLVED ENERGY FLUX MEASUREMENTS IN  
THE DIVERTOR OF THE ASDEX TOKAMAK BY COMPUTERIZED  
INFRARED THERMOGRAPHY

E.R. Müller, B.K. Bein<sup>+</sup>, K. Steinmetz

IPP III/97

June 1984

---

<sup>+</sup>Institut für Experimentalphysik VI, Ruhr-Universität,  
Bochum, Federal Republic of Germany

*Die nachstehende Arbeit wurde im Rahmen des Vertrages zwischen dem  
Max-Planck-Institut für Plasmaphysik und der Europäischen Atomgemeinschaft über die  
Zusammenarbeit auf dem Gebiete der Plasmaphysik durchgeführt.*

Abstract

A new, fully computerized and automatic thermographic system has been developed. Its two central components are an AGA THV 780 infrared camera and a PDP-11/34 computer. The temperature profile of a single line can be recorded in real time with a repetition rate of 2500 Hz, a spatial resolution of 128 data samples per line and a signal resolution equivalent to a black-body temperature of  $0.2^{\circ}\text{C}$ . In the picture mode, 25 pictures with 64 lines each are recorded per second. The power fluxes absorbed by the ASDEX neutralizer plates are computed from the measured surface temperature evolution of the plates. For this purpose, a combined analytical-numerical method of solving the 1-dimensional heat diffusion equation for a solid of finite thickness bounded by two parallel planes was developed.

In high-density ( $\bar{n}_e = 8 \times 10^{13} \text{ cm}^{-3}$ ) neutral-beam-heated (L-mode) divertor discharges in ASDEX, the power deposition on the neutralizer plates is reduced to about 10-15 % of the total heating power, owing to the inelastic scattering of the divertor plasma from a neutral gas target. Between 30 % and 40 % of the power is missing in the global balance, presumably owing to partial reflection of the energy and particle fluxes incident on the neutralizer plates at grazing angles. The power flow inside the divertor chambers is restricted to an approximately 1-cm-thick plasma scrape-off layer. This width depends only weakly on the density and heating power. During H-phases free of Edge Localized Mode (ELM) activity the energy flow into the divertor is blocked. During H-phases with ELM activity the energy is expelled into the divertor in very short intense pulses (several MW for about one hundred  $\mu\text{s}$ ). Sawtooth events are able to transport significant amounts of energy from the plasma core to the peripheral zones and the scrape-off layer, and they are frequently correlated with transitions from the L to the H mode.

---

<sup>+</sup>Institut für Experimentalphysik VI, Ruhr-Universität,  
Bochum, Federal Republic of Germany

## Contents

	Page
1. Introduction	1
2. The thermographic system	2
2.1 The general design of the thermographic system	2
2.2 The infrared camera and recording, display and absolute calibration of IR data	4
2.3 The ASDEX tokamak and experimental arrangement for thermographic measurements	8
3. Analysis of infrared detector signal	10
4. Results from infrared thermography in ASDEX	17
4.1 Global power balances	17
4.2 Power deposition profiles on the divertor neutralizer plates in neutral-beam-heated L-mode and H-mode discharges.	21
4.3 Modulation of energy fluxes in the scrape-off layer by sawtooth activity	24
5. Summary and conclusions	25
References	29



## 1. Introduction

One of the main objectives of present-day experiments in controlled nuclear fusion research is to study the energy loss mechanisms of magnetically confined plasmas in order to develop techniques for controlling them. The large tokamak experiments, ASDEX /1/, PDX /2/, and DOUBLET-III /3/, have demonstrated the capability of the axisymmetric poloidal divertor, as compared with the limiter, of significantly reducing the metallic impurity content of the main plasma and hence its power losses due to electromagnetic line radiation. About 80 % of the total loss power is diverted from the main chamber to the remote and separate divertor chambers. The major fraction of this power can be dissipated by inelastic scattering of the divertor plasma from a neutral gas target /1/. The residual power strikes the divertor neutralizer plates. Since this power deposition may occur non-uniformly on small areas and in short pulses, the erosion problem of divertor neutralizer plates will become severe in reactor-relevant tokamaks with high plasma power densities and discharge durations of about 10 seconds. In order to optimize the design of components exposed to high heat fluxes, an understanding of the heat flux pattern is essential.

Recently, a new plasma regime, called the H-mode, with improved particle and energy confinement was observed in ASDEX /4-6/. We shall show in this paper that a time and space-resolved investigation of the energy fluxes in the plasma scrape-off layer contributes to the understanding of this phenomenon. Preliminary results have been published in Ref. /7/.

For several years thermography has been used to determine the power deposition on high-heat-flux components in controlled fusion experiments /8/: an infrared camera measures the surface temperature evolution of the observed object, and from these data the deposited heat flux is computed by solving the heat conduction equation for the heat source at the surface. The advantages of the non-contact, remote-sensing method are obvious. One avoids all problems to which components mounted inside the tokamak are subject owing to high

temperatures, ultrahigh vacuum, high fluxes of neutron and gamma radiation, high magnetic fields and electric potentials. The thermographic measurements in nuclear fusion research published hitherto /8-15/ suffer from one or even several of the following disadvantages: Generally, only qualitative statements about power fluxes are deduced from the measured surface temperatures. Quantitative determination of power deposition is only available for single points in space, while for the spatial variation reasonable assumptions are made. The time resolution of analysis is usually also poor. Frequently, the time history of power deposition is approximated by a rather simple algebraic expression, and the surface temperature evolution calculated from it is fitted to the raw data. Assuming a semi-infinite solid for the heat-absorbing target, as was done in all experiments quoted, is only justified when the discharge durations do not exceed several hundred milliseconds.

We have developed a new, fully computerized thermographic system which does not need all these assumptions, approximations and omissions, but meets the requirements of a space resolution in the mm range, a time resolution better than half a millisecond, a temperature resolution of about  $0.2^{\circ}\text{C}$  and a dynamic range of several hundred degrees C. These stringent requirements are absolutely necessary in order to allow investigation of very important plasma processes, such as the transition from the L to the H-mode.

The thermographic system, the experimental arrangement in ASDEX and the absolute calibration are described in Sec. II of the paper. The computation of power fluxes from the surface temperature data of a plate with finite thickness is treated in Sec. III. Measurements in ASDEX are discussed in Sec. IV. The paper is summarized in Sec. V.

## 2. The thermographic system

### 2.1 The general design of the thermographic system

The thermographic system is depicted in Fig. 1 and a block diagram is shown in Fig. 2. The system is based on a commercially available infrared camera of the type AGA THV 780. During tokamak operation, the



camera and its power supply and control unit are placed immediately next to the tokamak in the experiment hall. After digitization, the IR signal is transmitted over a distance of about 50 m to the hardware mounted in two racks in the control area. The heart of this hardware is a PDP-11/34 computer. Since the computer is not fast enough to cope with real-time data acquisition, the digitized IR signal is preprocessed by specific hardware (data reduction etc.) and written into a dual access bulk storage which acts as a memory buffer. The computer reads the data from the bulk storage and sends them to the local archiving facilities, consisting of a 1.2 Mbyte disk for on-line storage and a magnetic tape for off-line storage. Vice versa, the computer has access to data on tape and disk and can write them into the bulk storage. From there the data are transmitted to a hardwired processor, which prepares them (data reduction, range spreading, etc.) for display. Then they are passed to two synchronized video controllers which form a video signal suitable for display by means of a common TV set.

Recording and display of IR data can be performed automatically and in different modes of operation specified by the computer software. The programs are selected on a control panel, where also various lamps announce the current status of the system. The computer terminal is another user interface. It serves for input of alphanumeric data and modification of software parameters controlling the recording or display process, and it permits listings of alphanumeric data and error codes.

There are connections to the ASDEX diagnostics control and to other diagnostics: The central ASDEX control system provides the current plasma discharge number, the time of day and trigger pulses from the central experiment timer. Up to 16 analog signals of other diagnostics, such as thermocouple calorimetry, are recorded by means of a 16-channel input multiplexer with A/D conversion.

Data analysis according to Sec. 3 is performed off-line on the more powerful PDP-11/70 main computer for ASDEX. Nevertheless, the thermographic system is equipped with its own PDP-11/34 computer for

the following reasons: This diagnostic requires fast acquisition of more than 300,000 data per second, generates a large total amount of data (up to 1.2 Mbyte per plasma discharge) and requires stand-alone operation. A link of the PDP-11/34 to the main computer system of ASDEX, which is described in detail in Ref. /16/, is presently undertaken. Since the two computers belong to the same family and use the RSX-11/M operating system and GALE (General Acquisition System for Laboratory Experiments /17/) as the central component of data acquisition software, the main computer and the thermographic system are hardware and software-compatible.

## 2.2 The infrared camera and recording, display and absolute calibration of IR data

After this more general survey, specific components and design aspects of the thermographic system are discussed in detail:

The infrared camera uses a liquid-nitrogen-cooled photovoltaic InSb detector sensitive to wavelengths between 2 and 5  $\mu\text{m}$ . With this single detector IR pictures are obtained by means of an optomechanical scanning system: two polygonal prisms rotate around perpendicular axes in front of the detector. A television-type raster, called a subframe and consisting of 70 lines, is produced with a repetition rate of 25 Hz. With interlaced scanning, four of these subframes form a complete frame with 280 lines.

By means of control electronics one of the two prisms can be stopped in a well-defined position corresponding to the centre line in the frame, thus switching the camera to the line scan operation mode. Now, the infrared emission profile of a single line is measured with a repetition rate of 2500 Hz.

The spatial resolution along the line amounts to 1/130 of the field of view of the camera lens. The temperature resolution depends on the camera aperture setting and on the emissivity and temperature of the object owing to the nonlinear response curve of the IR detector



(Fig. 3). For a black-body radiation source at room temperature and an aperture value of 1.8 the temperature resolution is  $0.2^{\circ}\text{C}$ . The dynamic range extends from  $-30^{\circ}\text{C}$  to  $750^{\circ}\text{C}$  (aperture value 20). Owing to the fact that the camera is mounted next to the experiment and is thus exposed to relatively high fluctuating magnetic fields (up to  $3\text{ V}\cdot\text{s}\cdot\text{m}^{-2}$ ), the standard magnetic position-sensing heads of the camera prisms are replaced by optical ones.

The principal design feature of the digital part of the thermographic system is that it retains the essential technical data of the IR camera, such as space, time and temperature resolution. Hence, for digitization of the camera signal over its full dynamic range and in real time, an analog-digital converter with 11-bit resolution and a sampling interval of  $2.4\text{ }\mu\text{s}$  is employed. A preamplifier is activated when a temperature resolution of  $0.2^{\circ}\text{C}$  is required.

The dual access bulk storage has a capacity of 512 kbytes. The first port is connected to the PDP-11/34, while the second one is for read-in and read-out of data. Before data acquisition the bulk storage is initialized by the PDP-11/34, but during data acquisition it is independent of computer control.

For a given sample in the picture frame, its address in the bulk memory is uniquely defined. Exact determination of this address and simultaneous triggering of the A/D converter are realized by a control unit synchronized with the camera by the output pulses of the position-sensing heads of the camera prisms. A single line is resolved into 128 samples. A complete frame, consisting of four subframes with  $64 \times 128$  samples each, needs a storage capacity of 32 kwords.

Since the writing into the bulk storage and the reading to the disk occur at the same time - the latter at a much slower rate - the recording capacity is limited by the bulk storage only when full time resolution is required. When data reduction is performed, e.g. when only every tenth subframe (picture mode) or line (line scan mode) is stored on disk, the disk (1.2 Mbyte) limits the data amount.

The data are transferred from the disk to the magnetic tape after the acquisition phase. The structure of the data written on tape is prescribed by the general acquisition system GALE: The date, the time and the plasma discharge number are registered in the "header" of the "configuration file", the "data descriptor block" includes alphanumeric data and comments, the "module control block" contains parameters describing the total amount of data recorded and the degree of data reduction, and the "data block" consists of the IR detector response curve, the thermocouple array reading and the IR camera signal.

The signal displayed on the TV monitor is not the raw signal of the camera but the surface temperature of the object, which is computed by means of the nonlinear calibration curve (Fig. 3). In view of transmission and reflexion losses by lenses and windows and also air attenuation, a special operation mode is used for in-situ calibration: a cursor on the TV monitor marks up to 16 positions in the IR picture which correspond to the locations of thermocouples at the object. During a temperature variation of the object, the IR emission from the marked spots is correlated with the reading of the respective thermocouples at 16 preselectable time intervals. The linearly interpolated pairs of values for the IR emission and temperature form the calibration curve.

In the picture mode, the temperature signal is converted into 16 gray tones on the black-and-white TV monitor: hot object areas are light, cold areas are dark in tone. It is optional to replace the gray tones by 16 different colors of a color TV monitor. Since the 16 levels are equivalent to 4-bit resolution, either the information content of the 11-bit data has to be reduced or the temperature range spanned by the 16 gray tones has to be restricted. The latter, the selection of a smaller temperature window, can be performed either externally by the setting of two potentiometers or internally by a comparator circuit, which determines the maximum as well as the minimum of the data for adjustment of the complete gray tone scale to the actual temperature range. It should be stressed that the recorded data remain unchanged, but the data are manipulated only for display.



The memory of the video controller has a storage capacity of  $256 \times 256$  samples, whereas a recorded subframe consists of only  $64 \times 128$ . Consequently, one or two subframes are displayed simultaneously, according to whether higher time or space resolution is preferred, and each sample is multiply displayed on the TV monitor.

Line-scan recordings are displayed on the TV monitor as a temperature profile (temperature vs space coordinate) which develops with time. This is technically realized by the MDC 256 video controller, which has a signal resolution of 1 bit, i.e. which permits only a black/white display. The temperature profile to be displayed determines which of the  $256 \times 256$  memory cells are switched on (1) or off (0). The amplitude of the curve can be adjusted to the full height of the plot frame on the TV monitor either by external potentiometer setting or by internal maximum/minimum determination.

In order to allow a useful selection of recorded data for a quantitative and more detailed analysis (see Sec. 3), the thermographic system has different aids at its disposal:

- Manual as well as automatic adjustment of the gray tone scale (picture mode) or profile amplitude (line-scan mode).

- Still display of a single picture or line scan.

- Stepping the displayed picture or line scan in the forward and backward directions.

- Fast, movie-type presentation of line-scan data with 20 lines per second.

- Simultaneous display of several line scans.

- Superpositioning of a temperature profile on a displayed picture. The line is selected by a cursor on the TV monitor (not to be confused with line scan mode!).

- Data reduction: only every n-th subframe or line scan recorded is displayed.

- Display of text information on the TV monitor.

- A hard-copy device connected to the TV monitor and the computer terminal.

There are three modes of data display. The pictures or line scans taken by the camera appear as "real-time displays" on the TV monitor. The display of data recorded and already stored on disk is performed by "control display". Since these data are usually overwritten during the next plasma discharge, this means that, firstly, they have to be copied on tape before and, secondly, only the last discharge is accessible by "control display". Owing to the high speed required during acquisition, the data have to be written on disk not in a file-oriented structure but in a physical format. For the "display of archived data", written on tape in file format, they are transferred to disk by the PIP utility. From this it follows that data acquisition and "control display", on the one hand, and "display of archived data", on the other, are mutually exclusive.

As stated above, the thermographic system is equipped with different operation modes for data recording and each one is realized by specific software. As the names of two important modes - "external clock" and "internal clock" - imply, the exact timing of successive subprograms is controlled, in the first case, by trigger signals provided by an external clock and, in the second case, by preprogrammed time marks of the internal computer clock. The total number of pictures (line scans) and the interval between recorded pictures (line scans) is to be preprogrammed. "External clock" is employed for routine recording during ASDEX plasma discharges.

### 2.3 The ASDEX tokamak and experimental arrangement for thermographic measurements

ASDEX is a large tokamak combining a double-null poloidal divertor with a near-circular shape of the interior magnetic flux surfaces ( $R = 1.65$  m,  $a = 0.40$  m). In addition to the ohmic heating power ( $\leq 0.5$  MW), up to 3.1 MW of neutral-injection power can be applied to the plasma for a time interval of 0.2 s: two neutral beams are injected parallel to the ohmic current (co-injection) into the  $H^+$  or  $D^+$  plasma with a kinetic energy of 40 keV. If not stated otherwise, the discharges are ungettered. Typical plasma parameters are reported in



Refs. /4-6/. In Fig. 4 a poloidal cross-section of the main chamber and the upper divertor with the arrangement of diagnostics, used for discussion in Sec. 4, is shown.

Since the electromagnetic stray fields in the vicinity of the tokamak are rather large (see Sec. 2.2), the infrared camera must be magnetically shielded and mounted at a distance of at least 2 m from the neutralizer plates. This makes optical imaging necessary, as shown schematically in Fig. 5. The vacuum window and the two lenses are made of calcium fluoride ( $\text{CaF}_2$ ). This material combines the advantages of extreme hardness and a high melting point, transmissivity from the vacuum ultraviolet to the infrared ( $0.12 - 10 \mu\text{m}$ ) and cheapness. In addition, two mirrors made of aluminium are used for optical alignment and rotation of the horizontal line-scan direction of the camera by  $90^\circ$  in the vertical z-direction. The spatial resolution of this imaging optics amounts to 1.7 mm on the neutralizer plate, which is about 1 % of the height of the plate. Figure 6, which shows a typical surface temperature profile along the vertical direction of the neutralizer plate, demonstrates that this spatial resolution is sufficient. Bore-holes on the neutralizer plate, appearing as dark points in the IR picture, provide spatial orientation.

Absolute calibration of the thermographic system is allowed by a thermocouple array mounted on the rear side of the neutralizer plate (Fig. 4). Since the metal tarnishes in the course of time and is also coated by a very thin titanium layer owing to occasional titanium gettering, its emissivity  $\epsilon$  is rather high, being about 0.55. It should be noted that, though the neutralizer plates show a color variation in the visible, the infrared emissivity just varies by less than 15 % over the entire area observed by the camera. Admittedly, two things would be desirable: Firstly, a neutralizer plate which can be preheated with heating-wires would increase the sensitivity of the measurement and facilitate calibration work. Secondly, reference radiation sources at both locations, the neutralizer plate and the intermediate real image, would offer the possibility of discriminating signal distortions due to plasma IR emission and ambient interference.

### 3. Analysis of infrared detector signal

The thermographic system allows space and time-resolved measurement of the surface temperature  $T_0(x, z, t)$  of the neutralizer plate. The task of data analysis is to compute the corresponding area density of power  $P_0(x, z, t)$  deposited on the surface.

Measurements in the picture mode show that the temperature of the plate is uniform in the toroidal direction  $x$  and, secondly, the characteristic width of the temperature profile along the coordinate  $z$  parallel to the surface (Figs. 6 and 7) is much larger than the thickness ( $d = 2 \text{ mm}$ ) of the plate. Hence, the thermal behaviour of the plate is governed in first-order approximation by the 1-dimensional heat conduction equation

$$\partial T(y, t) / \partial t = D \partial^2 T(y, t) / \partial y^2, \quad (1)$$

where  $y$  is the coordinate perpendicular to the surface and  $D = K/\rho c$  are the thermal diffusivity, conductivity, mass density, and specific heat, respectively. The power deposition density  $P_0(t)$  is determined by solving eq. 1 for the heat flux density at the surface:

$$P_0(t) = -K [\partial T(y, t) / \partial y]_{y \rightarrow 0} \quad (2)$$

From this it follows that  $P_0(t)$  represents a net energy flux to the neutralizer plate which is, in general, not identical to the heat flux in the plasma sheath immediately in front of the plate surface: part of the incident energy flux is reflected (Sec. 4.1), consumed by plasma-wall interaction processes such as desorption and secondary electron emission, or re-emitted as thermal radiation. Part of the energy transport from the plasma to the solid is not due to thermal conduction and convection but to electromagnetic radiation as well as neutral particle losses of the plasma /1/.

Main assumptions inherent in eqs. 1 and 2 are:

There are no volume heat sources or sinks in the interior of the plate. This means that inductive heating or phase transitions (melting) are excluded.

The energy transfer between the plasma and solid takes place in an infinitely thin surface layer of the solid.

The neutralizer plate is treated as homogeneous and isotropic with a smooth surface. Surface layers with thermal properties different to those of the bulk material are not considered in our treatment.

The thermal conductivity  $K$ , the thermal diffusivity  $D$ , mass density  $\rho$  and specific heat  $c$  are assumed to be temperature-independent and given by literature values for the plate material (titanium alloy CONTIMET ALV 64):  $K = 0.0712 \text{ W} \cdot \text{cm}^{-1} \cdot ^\circ\text{C}^{-1}$ ;  $D = 0.0285 \text{ cm}^2 \cdot \text{s}^{-1}$ ;  $\rho = 4.43 \text{ g} \cdot \text{cm}^{-3}$ ;  $c = 0.5652 \text{ W} \cdot \text{s} \cdot \text{g}^{-1} \cdot ^\circ\text{C}^{-1}$ .

The typical duration of ASDEX discharges ( $t \sim 3\text{s}$ ) exceeds the temperature equalization time over the plate thickness  $\tau_{\text{eq}} = d^2/(2D) \sim 0.7 \text{ s}$ . Consequently, the model of the semi-infinite solid [8] commonly used in thermographic data analysis does not apply, but the model of a solid bounded by two parallel planes is appropriate. The boundary and initial conditions for solving eqs. 1 and 2 are:

The time evolution of the front-surface temperature  $T_0(t)$  is prescribed by thermographic measurement:

$$[T(y,t)]_{y \rightarrow 0} = T_0(t). \quad (3)$$

The normal derivative  $\partial T_r(t)/\partial y$  of the rear-surface temperature is assumed to vanish. This is equivalent to the assumption of negligible heat losses on the time scale of the discharge duration:

$$P_r(t) = -K[\partial T(y,t)/\partial y]_{y \rightarrow d} = 0. \quad (4)$$

The time interval of about 10 minutes between successive ASDEX discharges guarantees uniform temperature distribution all over the plate at the beginning of each discharge:

$$T(y,t = 0) = T_0(t=0). \quad (5)$$



For the solution of the heat conduction problem (eqs. 1 and 2), a combined analytical-numerical method was developed /18,19/ which is based on a space-time dependent solution by means of Green's functions /20/:

$$T(y,t) = \frac{1}{\sqrt{\pi}} \int_0^t \frac{d\tau}{(t-\tau)} T_o(\tau) \sum_{n=-\infty}^{\infty} \frac{y+2nd}{2\sqrt{D(t-\tau)}} \exp \left[ -\frac{(y+2nd)^2}{4D(t-\tau)} \right] \quad (6)$$

$$- \frac{1}{\sqrt{\pi}} \int_0^t \frac{d\tau}{(t-\tau)} T_r(\tau) \sum_{n=-\infty}^{\infty} \frac{y+(2n+1)d}{2\sqrt{D(t-\tau)}} \exp \left[ -\frac{(y+(2n+1)d)^2}{4D(t-\tau)} \right].$$

From this expression the heat flux distribution in the plate can easily be derived:

$$P(y,t) = -K \partial T(y,t) / \partial y = \quad (7)$$

$$= - \frac{K}{2\sqrt{\pi D}} \int_0^t \frac{d\tau}{(t-\tau)^{3/2}} T_o(\tau) \left[ 1 - \frac{2y^2}{4D(t-\tau)} \right] \exp \left[ -\frac{y^2}{4D(t-\tau)} \right]$$

$$- \frac{K}{2\sqrt{\pi D}} \int_0^t \frac{d\tau}{(t-\tau)^{3/2}} T_o(\tau) \sum_{\substack{n=-\infty \\ n \neq 0}}^{\infty} \left[ 1 - \frac{2(y+2nd)^2}{4D(t-\tau)} \right] \exp \left[ -\frac{(y+2nd)^2}{4D(t-\tau)} \right]$$

$$+ \frac{K}{2\sqrt{\pi D}} \int_0^t \frac{d\tau}{(t-\tau)^{3/2}} T_r(\tau) \sum_{n=-\infty}^{\infty} \left[ 1 - \frac{2(y+(2n+1)d)^2}{4D(t-\tau)} \right] \exp \left[ -\frac{(y+(2n+1)d)^2}{4D(t-\tau)} \right].$$

The first term in eq. 7 corresponds to the solution of the semi-infinite solid /19/ and gives the major contribution to the surface

heat flux. This semi-infinite-solid term  $p^{sis}(y,t)$  can have a singularity at the boundary  $y=0$ , whereas the other two terms are without complications there. In order to avoid the singularity,  $p^{sis}(y,t)$  is expanded in powers of  $y-y'$  (Taylor series expansion), where  $y' > 0$  is an initially arbitrarily chosen location in the interior of the plate:

$$p^{sis}(y,t) = p^{sis}(y',t) + \frac{\partial p^{sis}(y',t)}{\partial y} (y-y') + \frac{1}{2} \frac{\partial^2 p^{sis}(y',t)}{\partial y^2} (y-y')^2 + \dots \quad (8)$$

Now, all terms on the right-hand side of eq. 8 are well defined owing to the fact that  $T(y,t)$  and  $\partial T(y,t)/\partial y$  (eqs. 6 and 7) and the higher derivatives with respect to  $y$  are continuous functions of  $y$  and  $t$  in the interior of the plate  $0 < y < d$ . In the limit  $y \rightarrow 0$  one then obtains the contribution of the semi-infinite-solid term to the total surface heat flux, which is given by

$$P(y \rightarrow 0, t) = P_o(t) = \quad (9)$$

$$\begin{aligned} &= - \frac{K}{2\sqrt{\pi D}} \int_0^t \frac{dT_o(\tau)}{(t-\tau)^{3/2}} \left[ 1 + \frac{4y'^2}{4D(t-\tau)} - \frac{4y'^4}{(4D(t-\tau))^2} + \dots \right] \exp \left[ - \frac{y'^2}{4D(t-\tau)} \right] \\ &- \frac{K}{2\sqrt{\pi D}} \int_0^t \frac{dT_o(\tau)}{(t-\tau)^{3/2}} \sum_{\substack{n=-\infty \\ n \neq 0}}^{\infty} \left[ 1 - \frac{2(2nd)^2}{4D(t-\tau)} \right] \exp \left[ - \frac{(2nd)^2}{4D(t-\tau)} \right] \\ &+ \frac{K}{2\sqrt{\pi D}} \int_0^t \frac{dT_r(\tau)}{(t-\tau)^{3/2}} \sum_{n=-\infty}^{\infty} \left[ 1 - \frac{2((2n+1)d)^2}{4D(t-\tau)} \right] \exp \left[ - \frac{((2n+1)d)^2}{4D(t-\tau)} \right] . \end{aligned}$$

After transformation of the integration variable  $\tau$ , the net power deposited on the surface can be written as

$$\begin{aligned}
 P_o(t) = & -\sqrt{\frac{Kgc}{4\pi}} \frac{4\sqrt{D}}{y'} \int_{y'/2\sqrt{Dt}}^{\infty} d\mu T_o(t-y'^2/4D\mu^2) w_{sis}(\mu, i) \\
 & -\sqrt{\frac{Kgc}{4\pi}} \frac{4\sqrt{D}}{d} \int_{d/2\sqrt{Dt}}^{\infty} d\mu T_o(t-d^2/4D\mu^2) w_d(\mu) \\
 & +\sqrt{\frac{Kgc}{4\pi}} \frac{4\sqrt{D}}{d} \int_{d/2\sqrt{Dt}}^{\infty} d\mu T_r(t-d^2/4D\mu^2) w_r(\mu),
 \end{aligned} \tag{10}$$

where the function  $w_{sis}(\mu, i)$  is given by

$$w_{sis}(\mu, i=2) = (1 + 4\mu^2 - 4\mu^4) \exp(-\mu^2) \tag{11}$$

or

$$w_{sis}(\mu, i=3) = (1 + \mu^2 + 8\mu^4 - 4\mu^6) \exp(-\mu^2). \tag{12}$$

Here  $i$  is the number of terms employed in series expansion for numerical computation. The functions  $w_d(\mu)$  and  $w_r(\mu)$  are defined by

$$w_d(\mu) = \sum_{\substack{n=-\infty \\ n \neq 0}}^{\infty} [1 - 2(2n)^2 \mu^2] \exp[-(2n)^2 \mu^2] \tag{13}$$

and

$$w_r(\mu) = \sum_{n=-\infty}^{\infty} [1 - 2(2n+1)^2 \mu^2] \exp[-(2n+1)^2 \mu^2]. \tag{14}$$

In numerical experiments of prescribed power deposition  $\rightarrow$  computation of the resulting surface temperature  $\rightarrow$  theoretical reproduction of the assumed power deposition, the convergence of the expansion solution was tested and optimized by adjusting the expansion parameter  $y'$  and the number of terms  $i$  to be used in the Taylor expansion /18,19/. For example, for sampling intervals of  $0.004 \leq \Delta t_m/s \leq 0.008$  and a thermal diffusivity  $D \approx 0.03 \text{ cm}^2/s$ , optimal results combining convergence and resolution efficiency are obtained for  $2 \leq i \leq 3$  and  $0.01 \leq y'/\text{cm} \leq 0.03$ , which means that the relation  $y' \approx \sqrt{2D\Delta t_m}$  is approximately satisfied. It should be stressed that for a given neutralizer plate material, characterized by its thermal diffusivity  $D$ , the values of  $y'$  and  $i$ , associated with the time interval  $\Delta t_m$ , have to be determined just once. The functions  $w_{sis}(\mu, i)$ ,  $w_d(\mu)$  and  $w_r(\mu)$  are tabulated for equidistant grid points, and during actual integration the values for arbitrary  $\mu$  are gained by fast linear interpolation.



In order to evaluate the power deposition  $P_0(t)$  on the front surface by means of eq. 10, a stable solution for the rear-surface temperature  $T_r(t)$  is needed. Using eq. 4 as boundary condition,  $T_r(t)$  is obtained from the global heat balance of the neutralizer plate during the entire course of time:

$$\int_0^t P_0(\tau) d\tau = \rho c \int_0^d [T(y,t) - T(y,t=0)] dy. \quad (15)$$

The result is

$$T_r(t) = \frac{\sqrt{D}}{K\sqrt{\pi}} \int_0^t \frac{d\tau P_0(\tau)}{(t-\tau)^{1/2}} \sum_{n=-\infty}^{\infty} \exp \left[ -\frac{((2n+1)d)^2}{4D(t-\tau)} \right]. \quad (16)$$

Equations 10 and 16 are two coupled integral equations. For rather thin plates with  $d \approx \sqrt{2D\Delta t_m}$  an iterative procedure is appropriate, whereas for thicker plates the two equations can be treated as decoupled by changing the upper integration limit in eq. 16 from  $t$  to  $t-\Delta t_m$ . After transformation of the integration variable, eq. 16 can be written in the form appropriate to numerical computation

$$T_r(t) = \frac{d}{K\sqrt{\pi}} \int_{d/2\sqrt{D\Delta t_m}}^{d/2\sqrt{D\Delta t_m}} d\mu P_0(t - d^2/4D\mu^2) w_p(\mu), \quad (17)$$

where  $w_p(\mu)$  is defined by

$$w_p(\mu) = \frac{1}{\mu^2} \sum_{n=-\infty}^{\infty} \exp[-(2n+1)^2 \mu^2]. \quad (18)$$

Figure 8 shows a result obtained by means of the 1-dimensional theory in the case of a plasma discharge heated by neutral-beam injection (L-mode /4/) during a time interval of 200 ms: From the measured surface temperature  $T_0(t)$ , both the rear-surface temperature  $T_r(t)$  and the power deposition density  $P_0(t)$  are computed. Despite the fact that

$T_0(t)$  rises continuously with time and slowly decays later, the very sharp onset of power deposition due to the start of injection heating and its abrupt drop at the end of neutral injection are clearly brought out. The rear surface of the neutralizer plate significantly heats up, and  $T_r(t)$  continues to grow even when the front surface has started cooling down. Figure 8 further demonstrates that radiation cooling of the plate can be neglected compared with the absorbed power density. Radiation cooling is only important for the temperature equalization between successive discharges.

The complete power deposition profiles  $P_0(z,t)$  (see Fig. 14) are computed by applying the 1-dimensional theory, discussed in this section, to the measured temperature profiles  $T_0(z,t)$ . This means that heat propagation parallel to the surface in the  $z$ -direction is neglected. The 1-dimensional analysis of the actually 2-dimensional problem can lead to systematic misinterpretations when sharply peaked power deposition profiles or localized bursts of high power loads have to be detected:

Sharply peaked power deposition profiles are broadened and flattened by the 1-dimensional power deposition calculations.

The heat propagation in the  $z$ -direction after localized bursts of high power load can be interpreted by the 1-dimensional treatment as retarded and sideways shifted power deposition [19].

Numerical simulations of surface heating due to localized power bursts and power deposition calculations comparing the 1 and 2-dimensional heat propagation in the plate are now undertaken in order to decide whether it is useful or not to apply the more accurate 2-dimensional treatment to the power deposition problem in ASDEX, at least to the transition from the L to the H-phase of neutral-beam-heated discharges (see Sec. 4.2).

#### 4. Results from infrared thermography in ASDEX

##### 4.1 Global power balances

In a divertor tokamak there are three main power loss channels from the plasma to the walls: (1) RAD: electromagnetic radiation and neutral particle losses to the walls of the main chamber; (2) RAD<sub>DIV</sub>: losses of the same type to the walls of the divertor chambers; both RAD and RAD<sub>DIV</sub> are measured with bolometers; (3) DEP: power deposition on the four divertor neutralizer plates due to thermal conduction and convection; DEP is measured by means of infrared thermography and (time-integrated) by thermocouple arrays (see Fig. 4). In order to evaluate the volume-integrated quantities RAD and RAD<sub>DIV</sub> from space-resolved radiation and neutral particle measurements, it is assumed that the emission is isotropic and uniform in the poloidal and toroidal directions. The thermographic determination of the power deposition DEP is obtained by surface-integration over all four neutralizer plates on the assumption of toroidal symmetry. To extrapolate from the radiation emission as well as power deposition, both measured in just one divertor zone (relating to one neutralizer plate), to the respective values in all four zones, it is assumed that the distribution among the four zones is identical to that of the electron line density  $\int n_{eDIV} dl$ , which is measured in front of each neutralizer plate. Spot checks on the latter assumption were made by vertically displacing the main plasma column and thus changing the distribution: A linear  $\int n_{eDIV} dl$  dependence of the energy deposition is verified in each of the four zones by thermocouple calorimetry (Fig. 9). In Ref. /1/ the linear scaling of RAD<sub>DIV</sub> with  $\int n_{eDIV} dl$  was discussed.

The dependence of the three power loss channels RAD, RAD<sub>DIV</sub> and DEP on the total heating power OH + NB during the steady state of neutral-beam-heated discharges in the L-mode is shown in Fig. 10a. The percentage contributions of the three loss channels to the total losses are almost independent of the heating power in the range from 0.4 to 2.0 MW. Figure 10b makes it evident that the global power balance changes much more drastically with the main plasma density  $\bar{n}_e$  than with the heating power: The divertor radiation grows exponentially with  $\bar{n}_e$  and attains maximum values of about 45 % of OH + NB. As a consequence, the power deposition on the neutralizer plates

is considerably reduced. Only the main plasma radiation RAD keeps within the limits of between 15 and 25 % of OH + NB.

Between 30 and 40 % of OH + NB is missing in the power balances depicted in Figs. 10a and 10b. There is a slight tendency for this value to increase with the heating power. The assumptions and approximations underlying the bolometric measurements are supported by the experimental experience that the sum  $RAD + RAD_{DIV}$  never exceeded 100 % of the heating power but, on the other hand, in some cases (with ohmic heating) could account for 80 to 90 % /1/. There are different sources of systematic error, which may become more important with the application of neutral-beam heating: charged particles following the magnetic field lines are not detected by the bolometers since they hit the aperture system, through which each bolometer looks perpendicularly onto a toroidal section of the plasma ring. For the same reason, fast neutral particles due to resonant charge exchange of ions are underestimated if they are emitted by preference in the toroidal direction. There are experimental indications that poloidal (divertor throats, stagnation points) and toroidal (gas valve) asymmetries exist.

A numerical model was developed /21/ which consists of a 1-dimensional electrostatic particle code for self-consistently calculating the particle trajectories and electric space-charge field in the plasma sheath region in the immediate vicinity of a material wall; in general, the sheath region is immersed in a magnetic field incident on the wall at an oblique angle. One main result obtained with this code is that the incidence angle of ions on the neutralizer plates for grazing incidence of the magnetic field ( $\sim 30^\circ$ ) becomes grazing as well. Reflection coefficients of ions in the kinetic energy range of 10 eV were derived /22/ by theoretical extrapolation from experimental results gained in the keV range. Despite the large error bar of the reflection coefficients also with respect to the unknown surface roughness of the neutralizer plates, a large fraction of the ions impinging on the plates at grazing incidence should be reflected more or less elastically as neutral particles in the forward direction. But



then these particles are not detected either by thermography, which is sensitive only to the net power absorbed by the plates (Sec. 3), or by bolometers, which are shielded against toroidally directed particles by collimators.

The tentative explanation for the missing power, namely that roughly half of the incident power is absorbed by the neutralizer plates whereas the other half is reflected and not detected, is additionally suggested by two experimental observations: Over large ranges of heating power and  $\bar{n}_e$  (Figs. 10a, 10b) the missing power is of the same magnitude as DEP. Secondly, the heat flux in front of the neutralizer plates, evaluated from Langmuir probe data [23], is twice as high as the thermographically determined power absorbed by the plates. The comparison between the two diagnostics is made at high plasma densities, since at low densities, corresponding to high temperatures and long mean-free paths, the energy fluxes calculated from Langmuir data become more uncertain and, apparently, too low. Probably, the assumptions entering the data analysis, based on a sheath model for the plasma surrounding the probe, are no longer valid: namely the assumptions of Maxwellian velocity distribution and temperature equalization between ions and electrons. It should be further stressed that the thermographic values are confirmed by thermocouple calorimetry: Since we know from thermography that the power deposition during the neutral-beam pulse can be stationary (see Fig. 8), power deposition values are derived in these special cases from thermocouple data by subtracting the signals of neutral-beam and ohmic discharges. From this agreement it is concluded that the assumptions, approximations and omissions inherent in thermographic data analysis (Sec. 3) are tolerable.

The characteristics of H-mode discharges which are now observed over a wide range of operating conditions are described in Refs. [4-6]. Roughly 50 ms after the start of neutral injection the discharge spontaneously changes into the H-mode. This transition to a plasma regime with improved energy and particle confinement results in an increase of  $\beta_p$  and  $\bar{n}_e$  but a sharp drop of several signals related to the energy and particle outflow into the divertor, such as the

hydrogen line radiation ( $H_{\alpha}$  line) in the divertor (Fig. 11). During the H-phase this  $H_{\alpha}$  light is modulated by characteristic bursts which are correlated with repetitive degradation of the energy and particle confinement of the main plasma. This MHD phenomenon is localized at the plasma periphery and is therefore called "Edge Localized Mode" (ELM)/6/. In this and the following section the influence of the L-H transition and of the ELMs on the global power balance and on the power deposition profiles at the divertor neutralizer plates will be discussed.

The time history of the power balance during an L-H transition is displayed in Fig. 11. (For this discharge the time resolution of the divertor bolometer was chosen as 20 ms in order to average the signal over the very short-lasting bursts. Every tenth line scan of the thermographic system with a time interval of 4 ms was recorded. Since the typical time interval between bursts is of the same order of magnitude, the bursts contribute to the calculated power deposition between bursts.) After a transition time of about 50 ms, the sum of the three power losses  $RAD$ ,  $RAD_{DIV}$  and  $DEP$  keeps roughly constant during the stationary L-phase, though individual loss channels show a variation with time. In the time interval 1.23 to 1.26 s all power losses drop sharply and  $\beta_p$  increases, which demonstrates that the energy confinement of the main plasma is improved. In the following H-phase the torus radiation increases and partly compensates the effect that the divertor radiation as well as the power deposition on the neutralizer plates are lower than in the L-phase. The power accountability becomes worse in the H-mode, even if one takes into account the energy released during the bursts.

Thermographic and bolometric measurements with improved time resolution ( $\sim 0.4$  ms) reveal that during the quiescent H-phases between bursts the power deposition on the neutralizer plate as well as the divertor radiation nearly vanish and are comparable to the ohmic level (Figs. 12 and 13). All power losses in the divertor via the two loss channels  $DEP$  and  $RAD_{DIV}$  arrive in bursts strongly time-correlated with the ELM activity. The power released by a single burst varies by almost one order of magnitude and depends on, for example, the burst

frequency. Particularly the last burst of the H-phase before re-transition into the L-phase is usually the most intense one. Maximum values of DEP of more than 10 MW have so far been observed. The total energy deposited during one burst with medium amplitude is roughly equal to the energy contained in a plasma annulus with a radius of 40 cm and a thickness of a few cm. For instance, with  $T_e(a) \approx 400$  eV,  $\bar{n}_e(a) \approx 8 \times 10^{12} \text{ cm}^{-3}$ ,  $a = 40$  cm,  $R = 165$  cm, annulus thickness  $\Delta = 2$  cm, its energy content amounts to about 260 Ws, a value which is consistent with frequently observed burst data of  $\Delta t_{\text{burst}} \approx 200 \text{ } \mu\text{s}$ ,  $\text{DEP}_{\text{burst}} \approx 1.3 \text{ MW}$ .

#### 4.2 Power deposition profiles on the divertor neutralizer plates in neutral-beam-heated L-mode and H-mode discharges

Figure 14 presents the power deposition profile across the neutralizer plate in the poloidal direction during the stationary phase of a neutral-beam-heated discharge in the L-mode. The power deposition profile is calculated from the measured surface temperature profile, which is of the type shown in Fig. 6, by applying 1-dimensional data analysis. The profile consists of one rather high and narrow peak centred at the intersection of the magnetic separatrix with the neutralizer plate. The asymmetry of the peak is characterized by a very steep decay towards lower values of the vertical coordinate  $z$  and a flatter exponential decay with growing  $z$ : the  $1/e$ -decay length of the energy flux scrape-off layer amounts to 7 mm (a 2-dimensional analysis would even yield a value 20 % smaller). Figure 15 demonstrates that the half-width (FWHM) of the peak, irrespective of its shape and including both wings, slightly decreases from 11 to 8 mm when the total heating power (OH + NB) is raised from 0.4 to 2.5 MW, and it is almost independent of the main plasma density  $\bar{n}_e$  within the range 1 to  $6 \times 10^{13} \text{ cm}^{-3}$ . The rather narrow energy flux width as well as its dependence on the total heating power agree well with theoretical results from the BALDUR transport code incorporating a self-consistent 1-dimensional scrape-off region model /24/, when it is assumed that electron heat conduction predominates in the energy flow parallel to the magnetic field lines in the scrape-off zone.

In Fig. 16 the vertical position  $z$  of the maximum of the thermographically determined power deposition profile is plotted as a function of time during a neutral-beam-heated discharge (L-mode). When neutral injection starts at  $t = 1.1$  s the plasma position feedback system increases the vertical magnetic field in order to counteract the outward shift due to the growing plasma energy content. The vertical field change again results in a shift of the intersection of the magnetic separatrix with the neutralizer plate. The separatrix contour and its intersection position can be calculated by means of a computer code /25/ using the signals received from magnetic pick-up coils. Figure 16 shows that the maximum of the measured power deposition exactly coincides with the calculated intersection of the magnetic separatrix and the neutralizer plate during the entire course of time, including transient phases between different heating regimes. The excellent agreement confirms that the energy flux from the main chamber to the divertor neutralizer plates is closely tied to magnetic flux surfaces. Recently, some deviations between the measured and calculated separatrix positions have been observed during long quiescent burst-free H-phases of discharges /26/.

The scrape-off layer narrows towards the divertor throat by a factor of about 4, compared with the width at the neutralizer plate, owing to the compression of magnetic flux surfaces. The actual high-temperature zone of the plasma within the throat thus has a width of only about 2 mm, this value being more than an order of magnitude smaller than the throat width of 3.7 cm. This is an important result which has to be taken into account in explaining the divertor impurity outflux through its throat /27/.

Radial profiles of temperature ( $T_{ed}$ ), density ( $n_{ed}$ ) and pressure ( $n_{ed}T_{ed}$ ) in the divertor scrape-off layer are measured by a Langmuir double probe (see Fig. 4) and, independently, by laser scattering diagnostics. All profiles show a pronounced peak located at the separatrix position, the width (FWHM) of which is between 2 and 3 cm in the case of the pressure profile. But there also appears to be a broad shoulder extending on the large major radius side to the last flux surface passing through the divertor throat /28/. Corre-



spondingly, the edge profiles of  $n_e$  and  $T_e$  in the torus midplane exhibit several distinct radial zones /29/: in the region close to the separatrix ( $0 < r - r_s < 2$  cm) the density fall-off length  $\lambda_n$  is 2 cm and the temperature fall-off length  $\lambda_T$  is 1 cm ( $\lambda_T$  slightly decreases with increasing heating power in the L-mode); in the outer radial zones the profiles flatten and both values,  $\lambda_n$  and  $\lambda_T$ , are larger. A comparison with the thermographic profiles allows one to conclude that the outer edge zones associated with the broad plasma shoulder in the divertor do not carry any substantial fraction of the energy flow to the neutralizer plates, but that this flow is concentrated in a narrow layer around the separatrix.

In Fig. 17 it is shown that the power deposition profiles during the H-phase of neutral injection are quite different compared with the L-phase. As stated above, during the quiescent H-phase between bursts the level of power deposition on the neutralizer plate is comparable to the ohmic level. Measurements with improved signal-to-noise ratio show that the same is true of the profile shape. In contrast, during the bursts, associated with excessive energy outflow from the main plasma into the divertor, the energy flux onto the neutralizer plates splits into several maxima located on both sides of the nominal separatrix. During a series of bursts, the distances of these maxima from the "separatrix" recur reproducibly as depicted in Fig. 18. Since  $n_e$  profile measurements with high time resolution at the plasma edge in the torus midplane, which are carried out by means of a 60 keV lithium beam /29/, do not show analogous phenomena, the generally well-defined magnetic field configuration, guiding the power flow, seems to burst open between the stagnation points and the divertor neutralizer plates during the ELMs.

#### 4.3 Modulation of energy flow in the scrape-off layer by sawtooth activity

##### L-type discharges

The influence of sawtooth activity on confinement is manifested as, for example, sharp steps in the density signals which are inverse to each other in the inner and outer radial plasma zones (Fig. 19). The loss of particles and energy from the plasma centre to the plasma periphery causes sharp rises also in the divertor  $H_{\alpha}$ -light signal. It is therefore to be expected that the energy fluxes within the divertor chamber are modulated in the same manner. In fact, this is found experimentally as displayed in Fig. 19 (bottom trace), where the spikes of the power deposition signal are strongly correlated with the sawteeth of the  $H_{\alpha}$  signal. In the discharge shown here ( $\bar{n}_e = 3.9 \times 10^{13} \text{ cm}^{-3}$ ,  $I_p = 380 \text{ kA}$ ,  $NB \approx 400 \text{ kW}$ ) one sawtooth causes an energy transfer to the neutralizer plates of the order of  $2 \times 10^3 \text{ J}$ , which is equivalent to about 5 % of the total energy content of the plasma.

##### H-type discharges

In the discharge displayed in Fig. 20 ( $\bar{n}_e = 3.8 \times 10^{13} \text{ cm}^{-3}$ ,  $I_p = 380 \text{ kA}$ ,  $NB \approx 800 \text{ kW}$ ) sawtooth (1) leads - as discussed above - to a sharp increase of the  $H_{\alpha}$ -light intensity in the divertor and of the power deposition on the neutralizer plates as well, while the discharge remains in the L-phase. It was reported /5/ that H-phases can be initiated by single sawtooth events when the neutral-beam injection power is above a certain level. Figure 20 gives an example: During sawtooth (2) the  $H_{\alpha}$  signal now sharply drops and the power deposition on the neutralizer plates, which has strongly increased since the first sawtooth, is drastically reduced. These findings make it evident that, in contrast to sawtooth (1), sawtooth (2) has not degraded the confinement of the bulk plasma but has even triggered the transition into the H-regime with improved confinement. This phase, however, only lasts for a short period. Not every subsequent sawtooth

in Fig. 20 gives rise to an L-H transition. The decisive criterion for such transitions is still under investigation.

## 5. Summary and conclusions

A new, fully computerized thermographic system for application in controlled nuclear fusion research has been developed. Its two central components are an infrared camera of the type AGA THV 780 and a PDP-11/34 computer.

The system is capable of recording either 25 interlaced infrared pictures, with 64 lines each, or 2500 infrared emission profiles of a single line per second. Each line is resolved into 128 samples. The signal resolution, in terms of equivalent temperature rise of a black body at room temperature, amounts to about  $0.2^{\circ}\text{C}$ , and the dynamic range of measurable black-body temperatures extends from room temperature to  $750^{\circ}\text{C}$ . In order to achieve these technical properties, the IR signal of the camera is digitized over its full dynamic range with 11-bit resolution and is processed in real time. The data are stored on-line on a 1.2 Mbyte disk and off-line on a magnetic tape. For display on a common TV monitor, they are converted, firstly, to a temperature signal by means of the nonlinear calibration curve and, secondly, either to 16 different gray tones/colors in the picture mode or to the shape of a curve in the line-scan mode.

The recording and display of IR data runs fully automatically in different modes of operation and is controlled by computer software. The thermographic system consists of commercially available standard components as far as possible. This allows its integration as a subsystem into a larger main system, such as the general ASDEX data acquisition system. On the other hand, the modular design of the thermographic system makes stand-alone operation of sub-components possible and offers great flexibility to changing requirements.

The digitized data, stored on magnetic tape, are directly accessible to the ASDEX main computer PDP-11/70 for analysis, i.e. for

computation of the area density of the power deposition on the object surface. The analysis is based on the solution of the 1-dimensional heat diffusion equation for a solid of finite thickness bounded by two parallel planes. The heat diffusion equation is solved for the time evolution of the heat flux absorbed at the surface. The thermographically measured surface temperature evolution is used as a boundary condition. The solution is composed of analytic expressions using space and time-dependent Green's functions. The method is not limited to short plasma discharge durations and does not require any assumptions about the time dependence of heat fluxes, but the spatial heat flux distribution in discharges with pulse lengths of several seconds can be determined with a time resolution in the ms range.

Thermography significantly contributes to the investigation of the power balance for neutral-beam-heated divertor discharges in ASDEX. During the steady state of L-mode discharges, 80 % of the heating power flows into the divertor. The splitting ratio between the two divertor power loss channels, the bolometrically detected radiation and neutral particle emission of the plasma ( $RAD_{DIV}$ ) and the thermographically detected power deposition onto the neutralizer plates (DEP), is nearly independent of the heating power but depends sensitively on  $\bar{n}_e$ : Since  $RAD_{DIV}$  grows exponentially with  $\bar{n}_e$ , DEP is considerably reduced to values of between 10 and 15 % of the heating power.

The power not accounted for in the global balance ranges between 30 and 40 % of the heating power in the L-mode. It shows a slight tendency to increase with the heating power and it is larger in the H-mode. A tentative explanation of the missing power is that roughly half of the power transported to the neutralizer plates by ions at grazing incidence is absorbed, whereas the other half is reflected in the forward direction and not detected.

In L-discharges, the power flow from the main plasma to the divertor neutralizer plates is restricted to a narrow layer closely tied to the magnetic separatrix contour. The power deposition profile on the

neutralizer plates consists of one asymmetric peak, the exponential decay of which outside the separatrix shows an  $1/e$ -length of 7 mm. The peak width is nearly independent of  $\bar{n}_e$ , and it decreases by 30 % when the heating power is raised by a factor of 6.

In the H-mode of neutral-beam-heated discharges the energy and particle confinement of the bulk plasma is improved, which results in an increased  $\beta_p$  value. During the quiescent H-phases without Edge Localized Modes (ELMs) both divertor power loss channels,  $RAD_{DIV}$  and DEP, become nearly negligible. The energy outflow of the bulk plasma seems to be blocked. Its radiation losses (RAD) due to impurity line radiation increase. Recent investigations show that, when the quiescent H-phase lasts sufficiently long, the discharge terminates owing to radiation collapse /30/. If, however, the ELM activity sets in before, the impurity radiation RAD can be sustained at a tolerable level. The energy confinement of the edge plasma is periodically degraded, i.e. the energy content of a peripheral plasma zone several cm thick is expelled into the divertor in repetitive, short bursts with durations of the order of 100  $\mu s$  and average powers in the MW range. During the bursts the energy deposition profile on the neutralizer plates bursts open into several maxima located on both sides of the nominal separatrix.

Sawtooth relaxations are generating heat pulses propagating from the plasma centre to the edge, into the scrape-off layer and, finally, to the divertor neutralizer plates. About 5 % of the total energy content of the plasma is deposited on the neutralizer plates during one sawtooth in the L-phase. Frequently, sawtooth events are correlated with transitions from the L to the H-mode. The crucial role which plasma edge temperature plays in attaining the H-regime was pointed out in Ref. /5/. It is very likely, that the amount of energy expelled from the plasma core by a sawtooth must be sufficiently large in order to raise the edge temperature above the H-mode threshold.



### Acknowledgement

The authors are indebted to their colleagues of the ASDEX team. They acknowledge the encouragement and support given by G. v. Gierke and M. Keilhacker (IPP Garching), M. Rosenberg and J. Pelzl (Ruhr-Universität Bochum). They wish to express their thanks to the ASDEX data acquisition group, particularly to N. Ruhs and D. Zimmermann, and to H. Niedermeyer for many fruitful discussions. They acknowledge the engineering work of R. Komen and the assistance of H. Wolf. Thanks are also due to H. Volkenandt for preparing the drawings and to I. Hermann for handling the secretarial work.

## References

- /1/ E.R. Müller, K. Behringer, H. Niedermeyer, Nucl. Fus. 22 (1982) 1651.
- /2/ R.J. Fonck, M. Bell, Jour. Nucl. Mat. 111 & 112 (1982) 343.
- /3/ M. Shimada, M. Nagami, K. Joki, S. Izumi, M. Maeno, Nucl. Fus. 22 (1982) 643.
- /4/ F. Wagner, et al., Phys. Rev. Lett. 49 (1982) 1408.
- /5/ F. Wagner, et al., Jour. Nucl. Mat. 121 (1984) 103.
- /6/ M. Keilhacker, et al., Plasma Physics and Controlled Fusion 26 (1984) 49.
- /7/ E.R. Müller, et al., Journ. Nucl. Mat. 121 (1984) 138.
- /8/ D.H.J. Goodall in Proc. of the 9th Symp. on Fusion Technology (Garmisch-Partenkirchen, 1976), Pergamon Press, Oxford (1976) 523; D.H.J. Goodall, in Proc of the Int. Symp. on Plasma Wall Interaction (Jülich, 1976), Pergamon Press, Oxford (1977) 53.
- /9/ R. Romain, Rev. Sci. Instr. 50 (1979) 1561.
- /10/ M. Maeno, K. Joki, S. Izumi, A. Kitsunozaki, M. Nagami, et al., Nucl. Fus. 21 (1981) 1474.
- /11/ T. Taylor, N. Brooks, K. Joki, Jour. Nucl. Mat. 111 & 112 (1982) 569.
- /12/ N. Miya, M. Shimada, et al., Jour. Nucl. Mat. 121 (1984) 126.
- /13/ T. Hino, J. de Grassie, T. Taylor, et al., Jour. Nucl. Mat. 121 (1984) 337.
- /14/ A.E. Pontau, W.B. Gauster, A.W. Mullendore, et al., Jour. Nucl. Mat. 111 & 112 (1982) 287.
- /15/ U. Samm, in Proc. 11th Europ. Conf. on Contr. Fus. and Plasma Physics (Aachen, 1983), Contr. Papers - Part II, 413.
- /16/ D. Zimmermann, N. Ruhs, H. Hohenöcker, in Proc. 12th Symp. on Fusion Technology (Jülich, 1982), Pergamon Press, Oxford (1983) 1461.

- /17/ R. Lathe, E. Müller, GALE System Programmers Manual, IPP Report R/27 (1978).
- /18/ B.K. Bein, E.R. Müller, J. Nucl. Mat. 111 & 112 (1982) 548.
- /19/ B.K. Bein, Derivation of the Power Deposition on Limiters and Divertor Targets from Thermographic Measurements, Ruhr-Universität Report, Bochum (1981).
- /20/ H.S. Carslaw, J.C. Jaeger, Conduction of Heat in Solids, Oxford University Press (1959).
- /21/ R. Chodura, Jour. Nucl. Mat. 111 & 112 (1982) 420.
- /22/ W. Eckstien, H. Verbeek, Data on Light Ion Reflection, IPP Report 9/32 (1979).
- /23/ Y. Shimomura, M. Keilhacker, K. Lackner, H. Murmann, Nucl. Fus. 23 (1983) 869.
- /24/ G. Becker, C.E. Singer, in Proc. IAEA Techn. Comm. Meeting on Divertor and Impurity Control, Garching (1981) 63.
- /25/ H. Winter, D.B. Albert, IPP Report 3/57, Garching (1980).
- /26/ U. Ditte, T. Grave, et al., to be published.
- /27/ G. Fussmann, W. Poschenrieder, et al., Journ. Nucl. Mat. 121 (1984) 164.
- /28/ G. Haas, et al., Journ. Nucl. Mat. 121 (1984) 151;  
E.B. Meservey, private communication.
- /29/ K. McCormick, et al., Journ. Nucl. Mat. 121 (1984) 48.
- /30/ P. Smeulders, M. Kornherr, E.R. Müller, to be published.

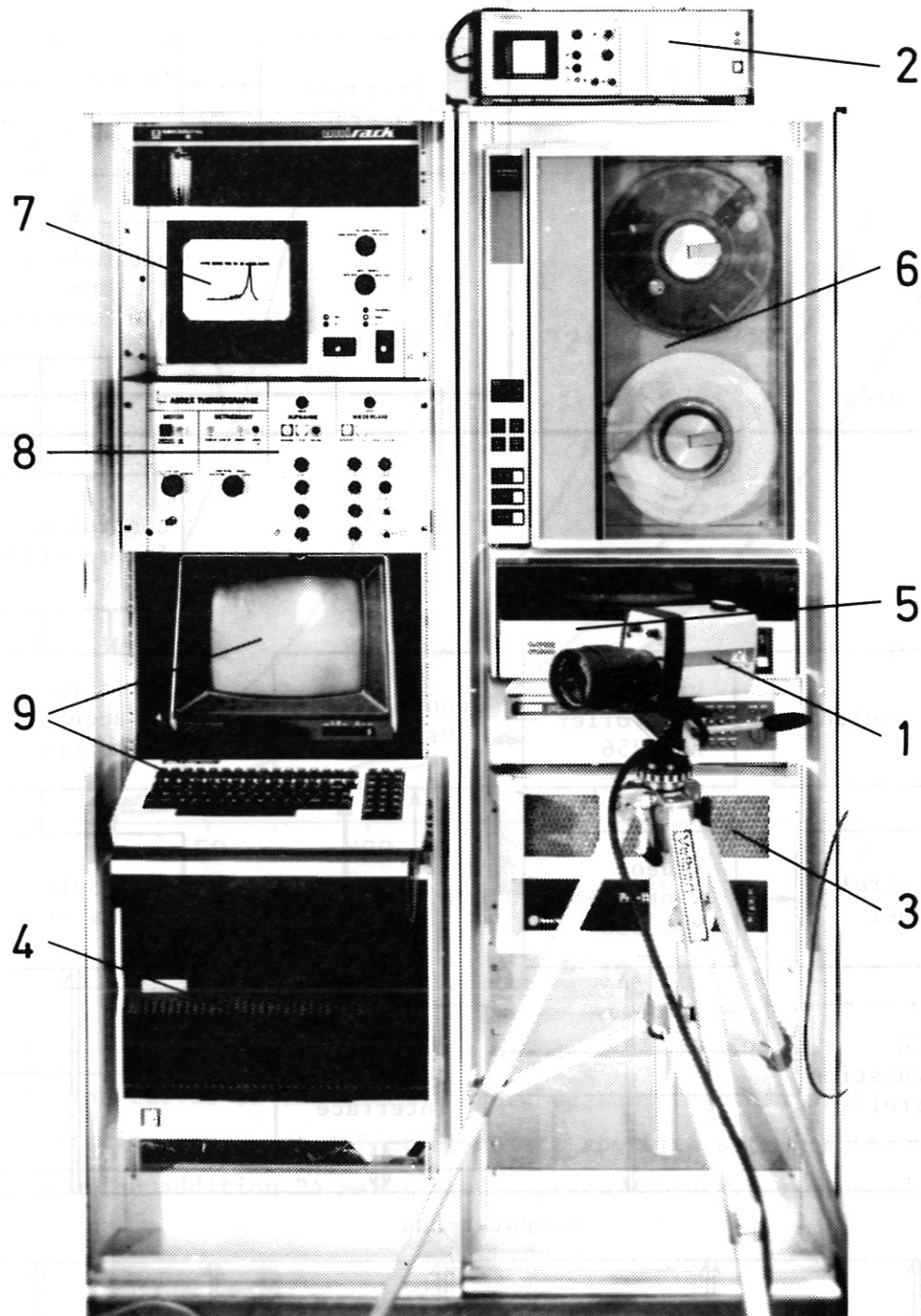


Fig. 1:

The thermographic system:

1. IR camera; 2. power supply and control unit for the camera;
3. PDP-11/34 computer; 4. dual access bulk store; 5. disk;
6. magnetic tape; 7. TV monitor; 8. control panel; 9. computer terminal.

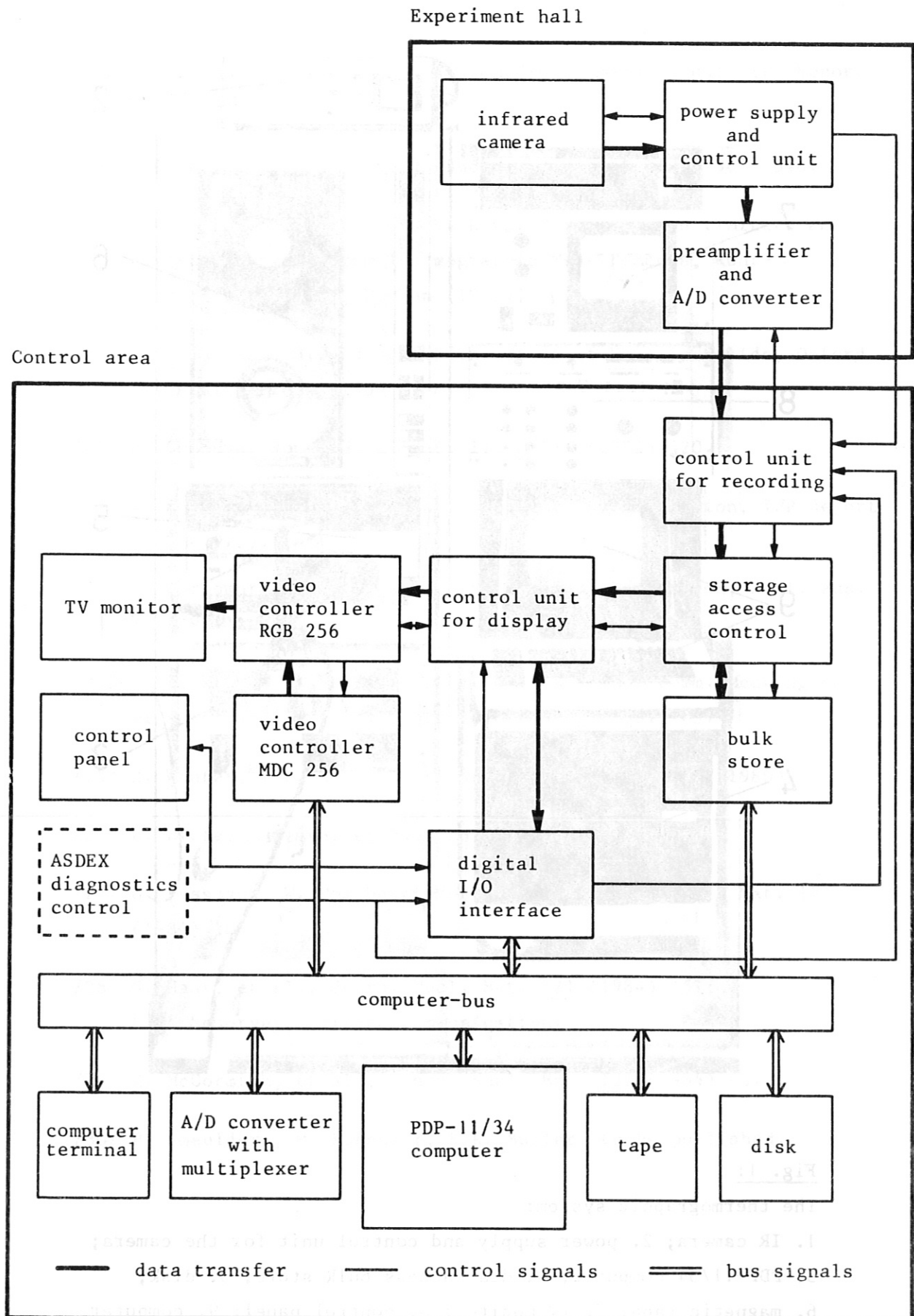


Fig. 2: General design of the thermographic system.



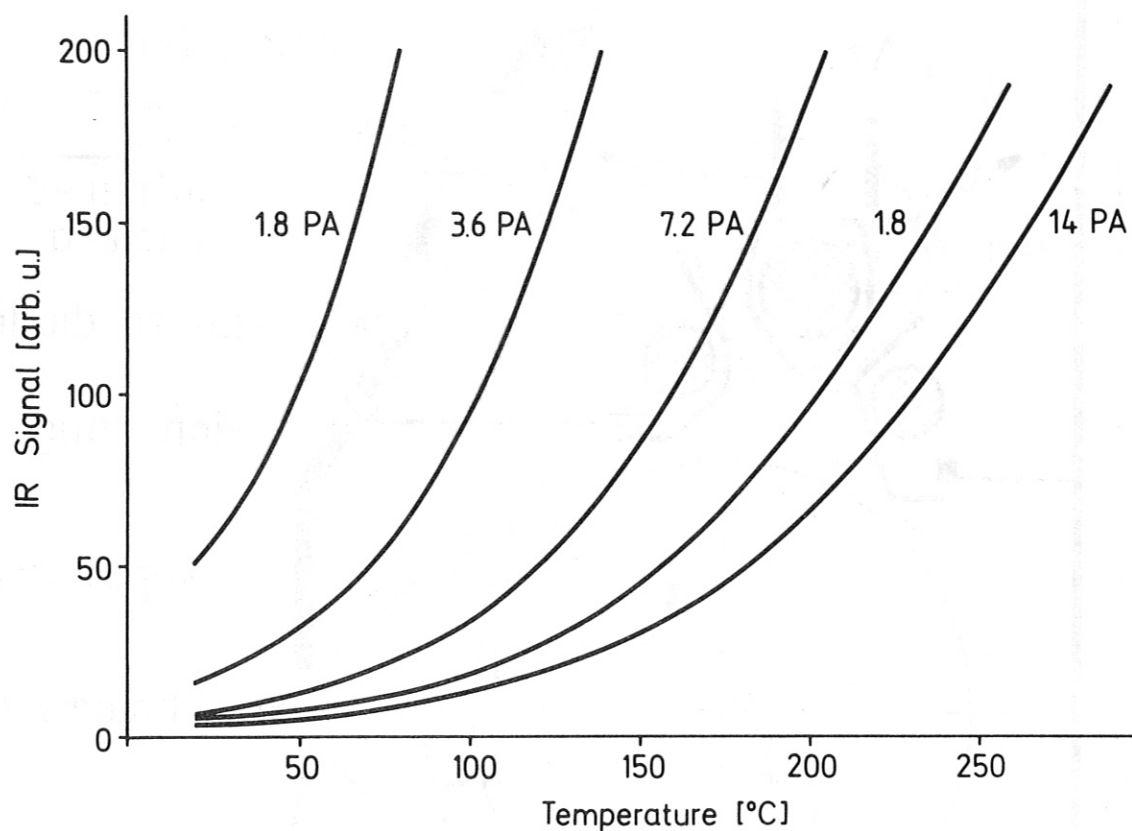


Fig. 3:

Calibration curves of the thermographic system, recorded with a black-body radiation source at different camera aperture settings (1.8, 3.6, 7.2, 14). The addition PA means that a preamplifier is activated.

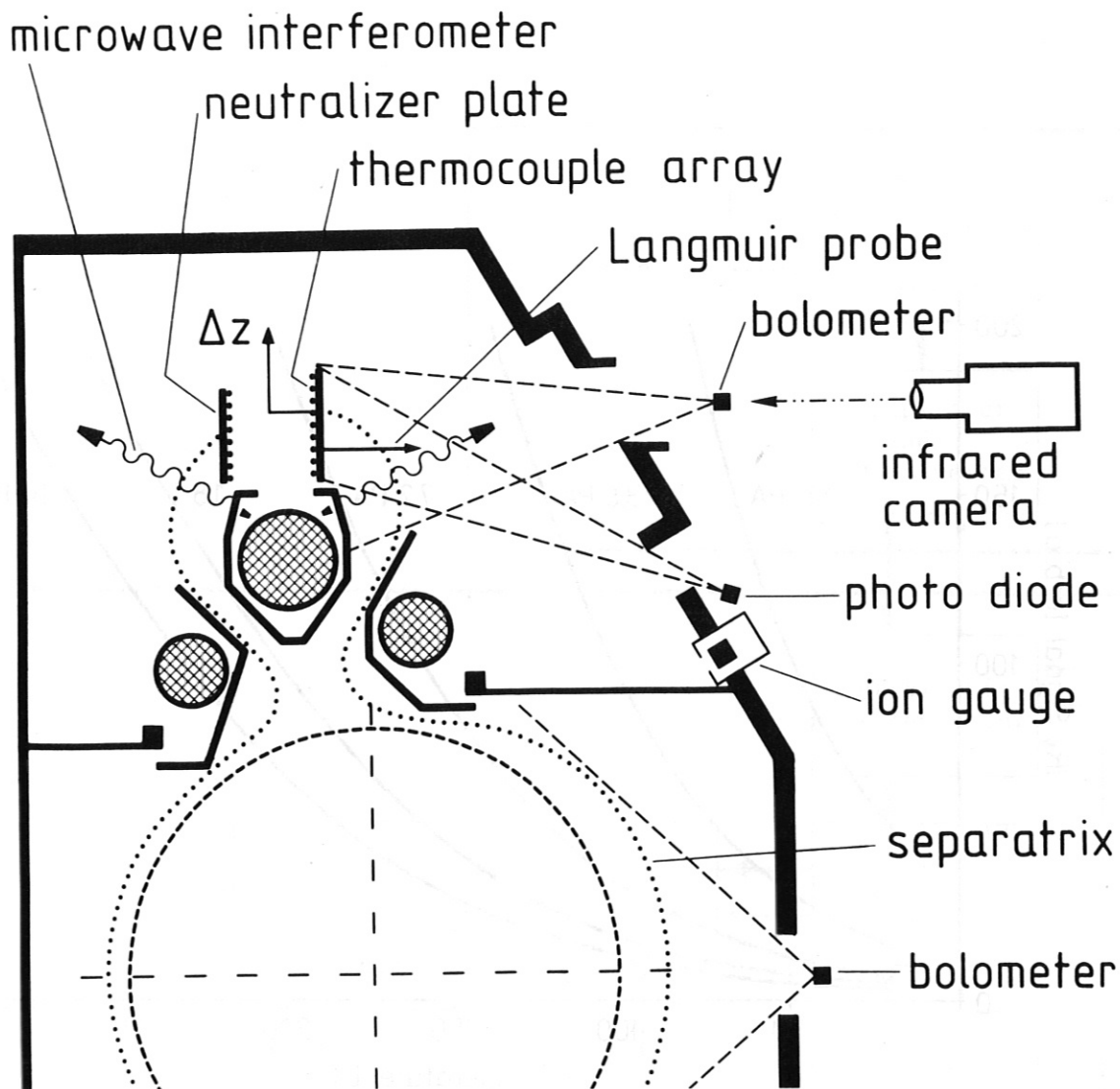


Fig. 4: Cross-sectional view of the ASDEX vessel with arrangement of diagnostics.

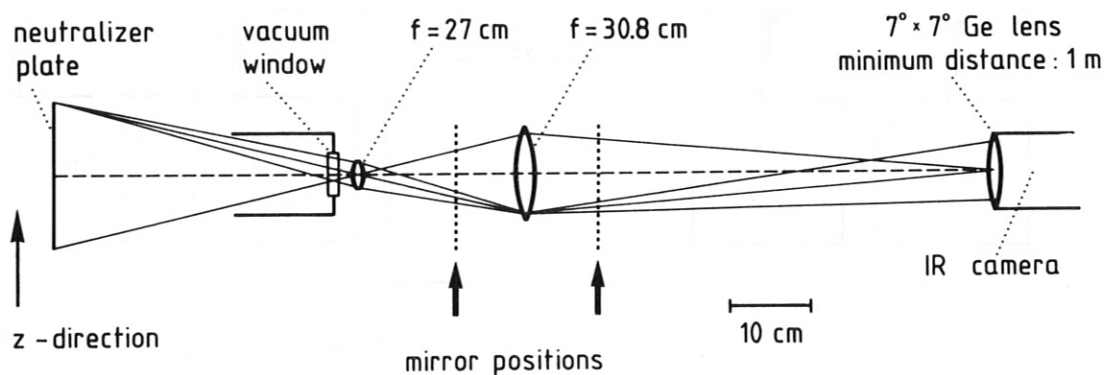
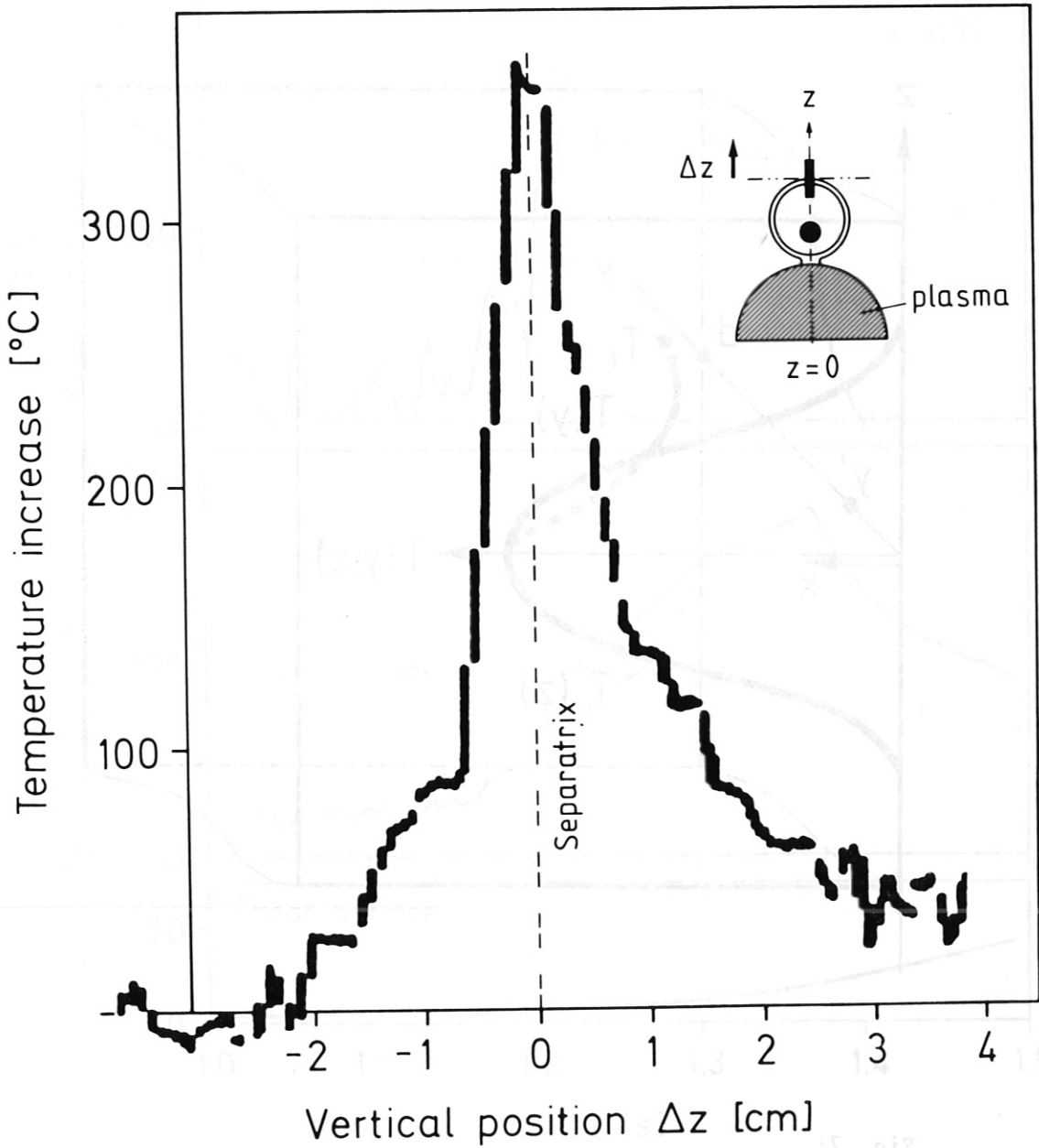
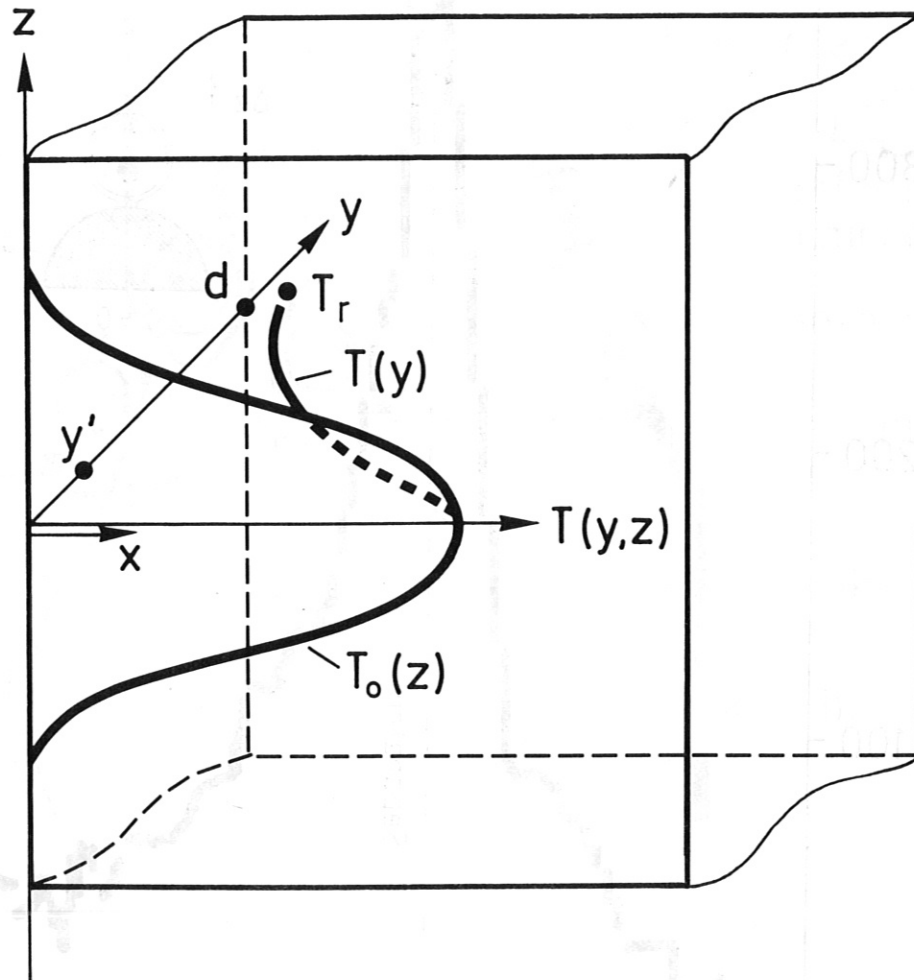


Fig. 5: Optical imaging of the divertor neutralizer plate with calcium fluoride lenses and aluminium mirrors.



**Fig. 6:** Surface temperature profile along the vertical direction of the neutralizer plate during the stationary phase of a neutral-beam-heated discharge in the L-mode ( $I_p = 400$  kA; OH + NB = 2.1 MW;  $\bar{n}_e = 2.8 \times 10^{13} \text{ cm}^{-3}$ )



**Fig. 7:**

Two-dimensional temperature distribution in the divertor neutralizer plate.

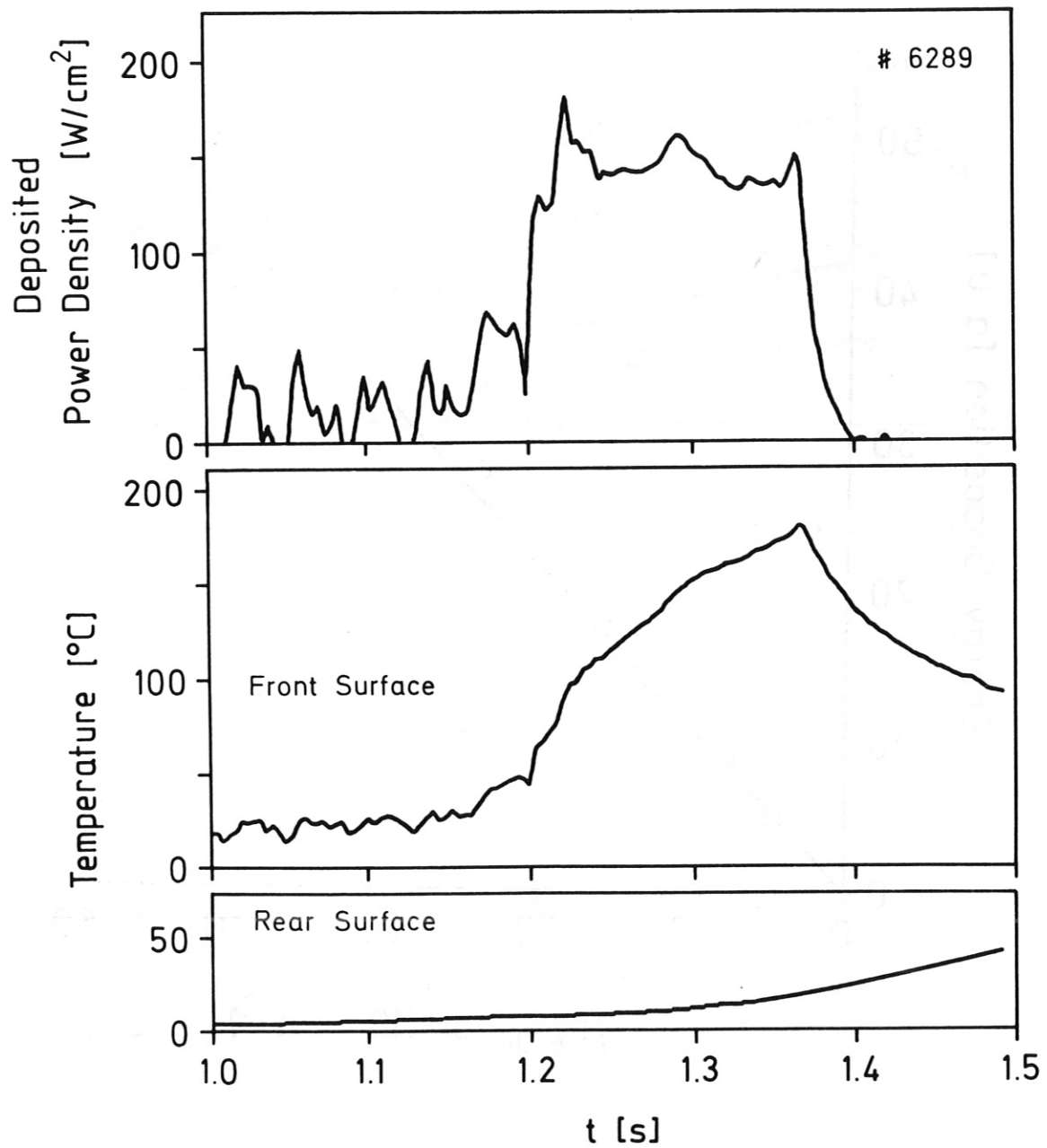


Fig. 8:

Time evolution of thermographically measured front surface temperature and calculated rear surface temperature as well as area density of power deposition on the front surface.



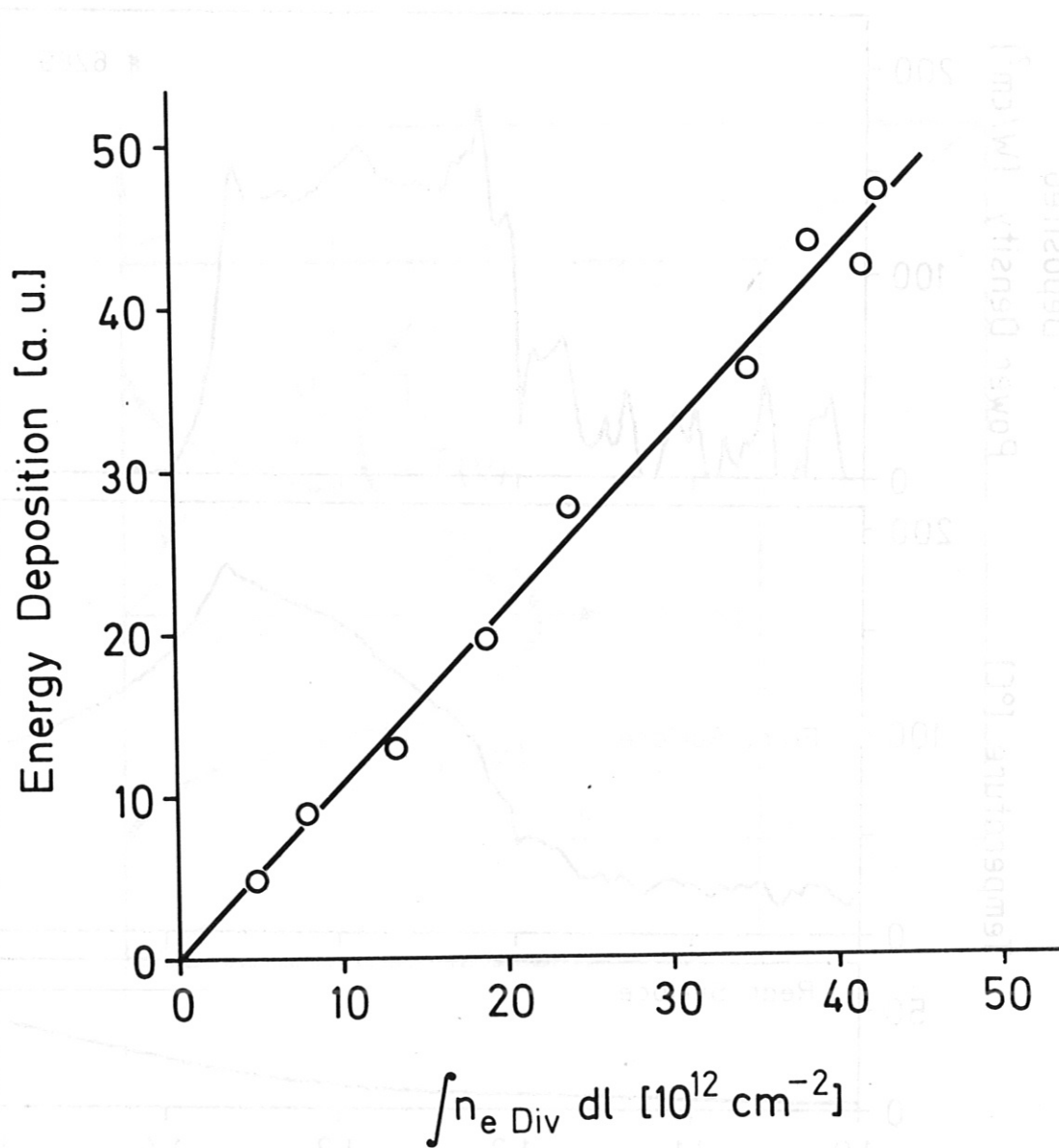


Fig. 9:

Calorimetrically determined energy deposition on the lower outer divertor neutralizer plate versus corresponding electron line density during a vertical shift of the plasma position from shot to shot.

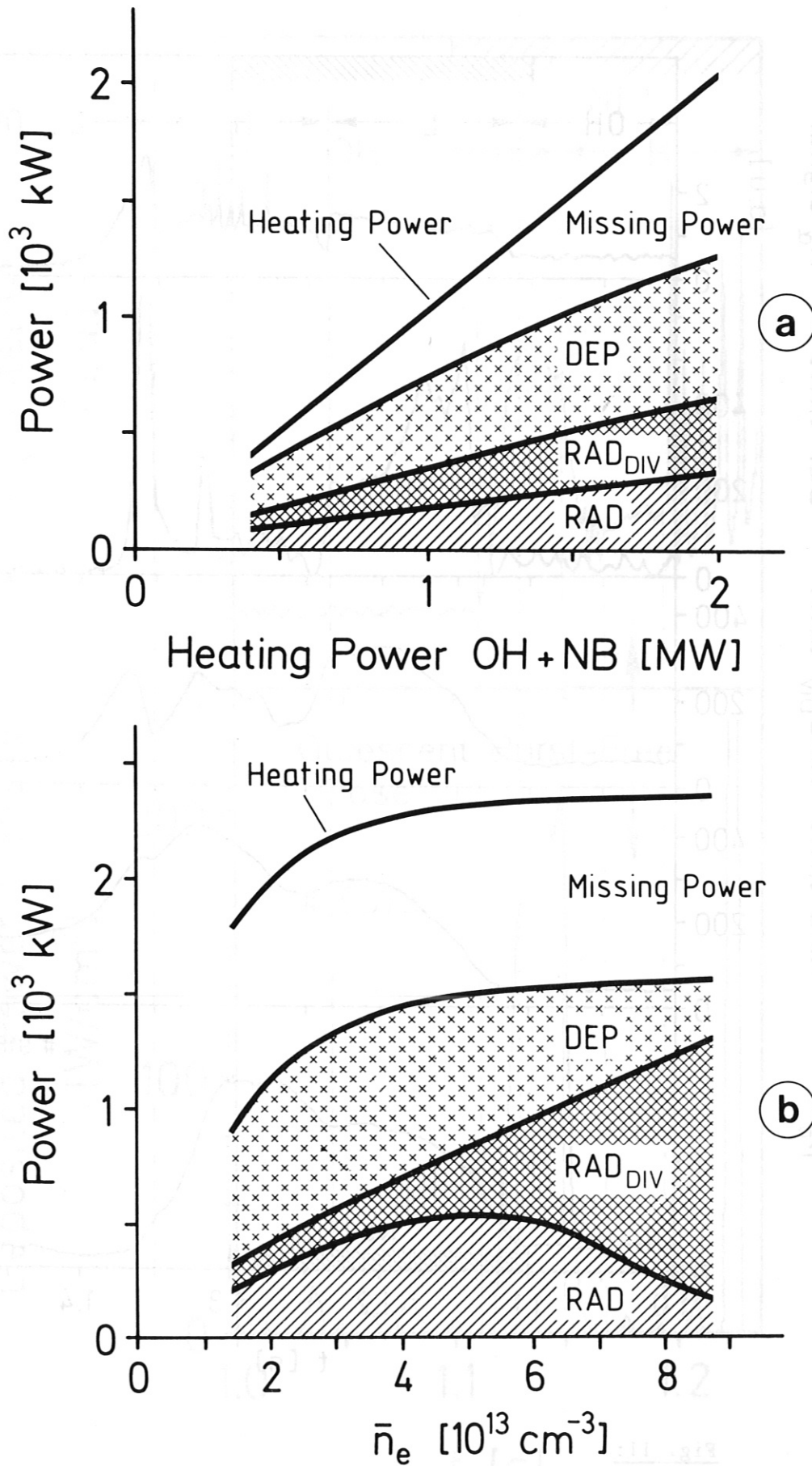


Fig. 10:

Variation of global power balance with (a) total heating power OH + NB ( $I_p = 380$  kA,  $\bar{n}_e = 2.8 \times 10^{13}$  cm<sup>-3</sup>),

(b) plasma density  $\bar{n}_e$  (OH + NB = 2.1 MW,  $I_p = 380$  kA).

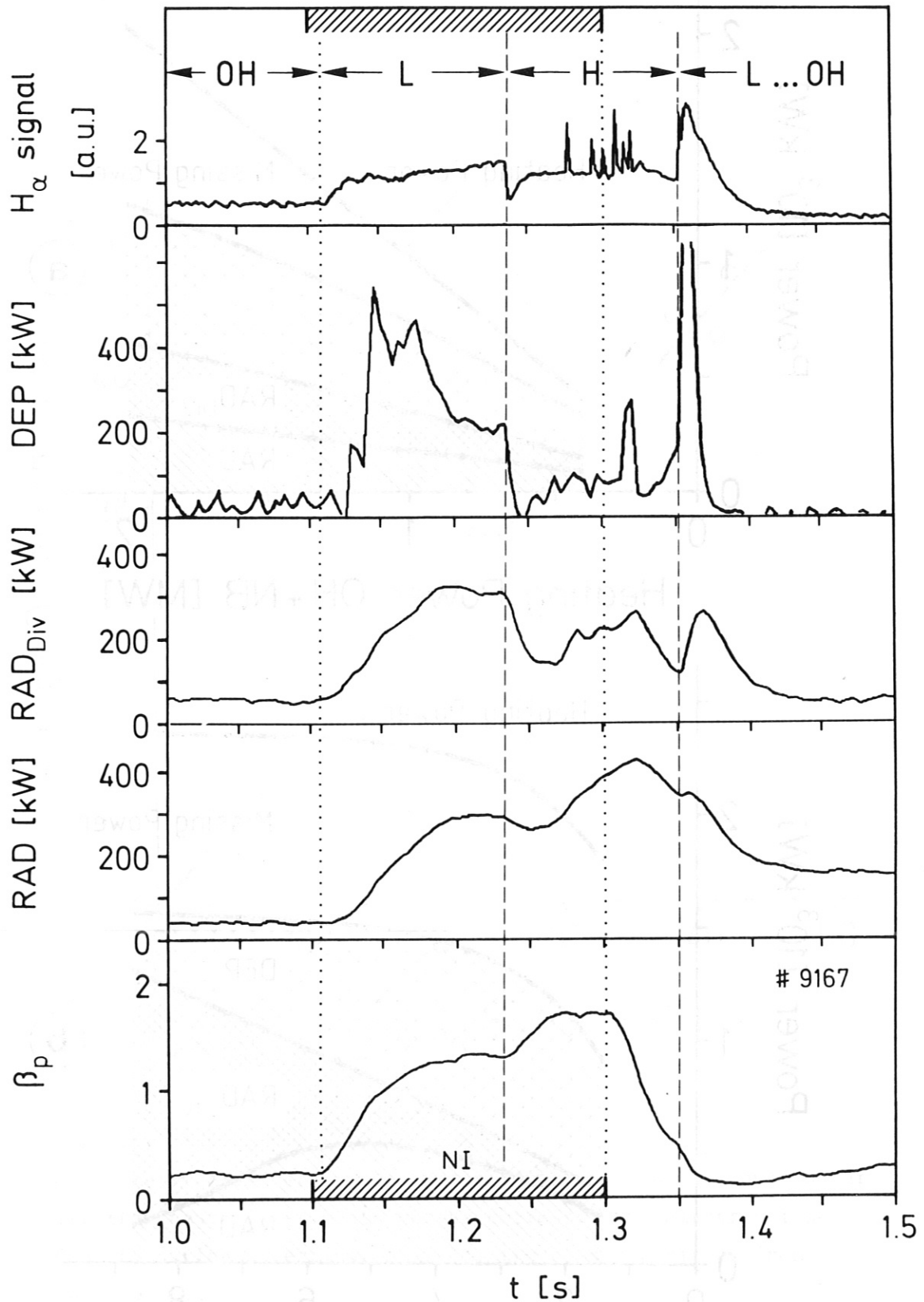


Fig. 11:

Time evolution of  $H_{\alpha}$  light from the divertor region, power deposition on the neutralizer plates, radiation from both divertor and main plasma, and  $\beta_p$  during a L-H transition ( $\bar{n}_e = 2.2 \times 10^{13} \text{ cm}^{-3}$ ,  $I_p = 300 \text{ kA}$ ,  $OH + NB = 2.1 \text{ MW}$ ).

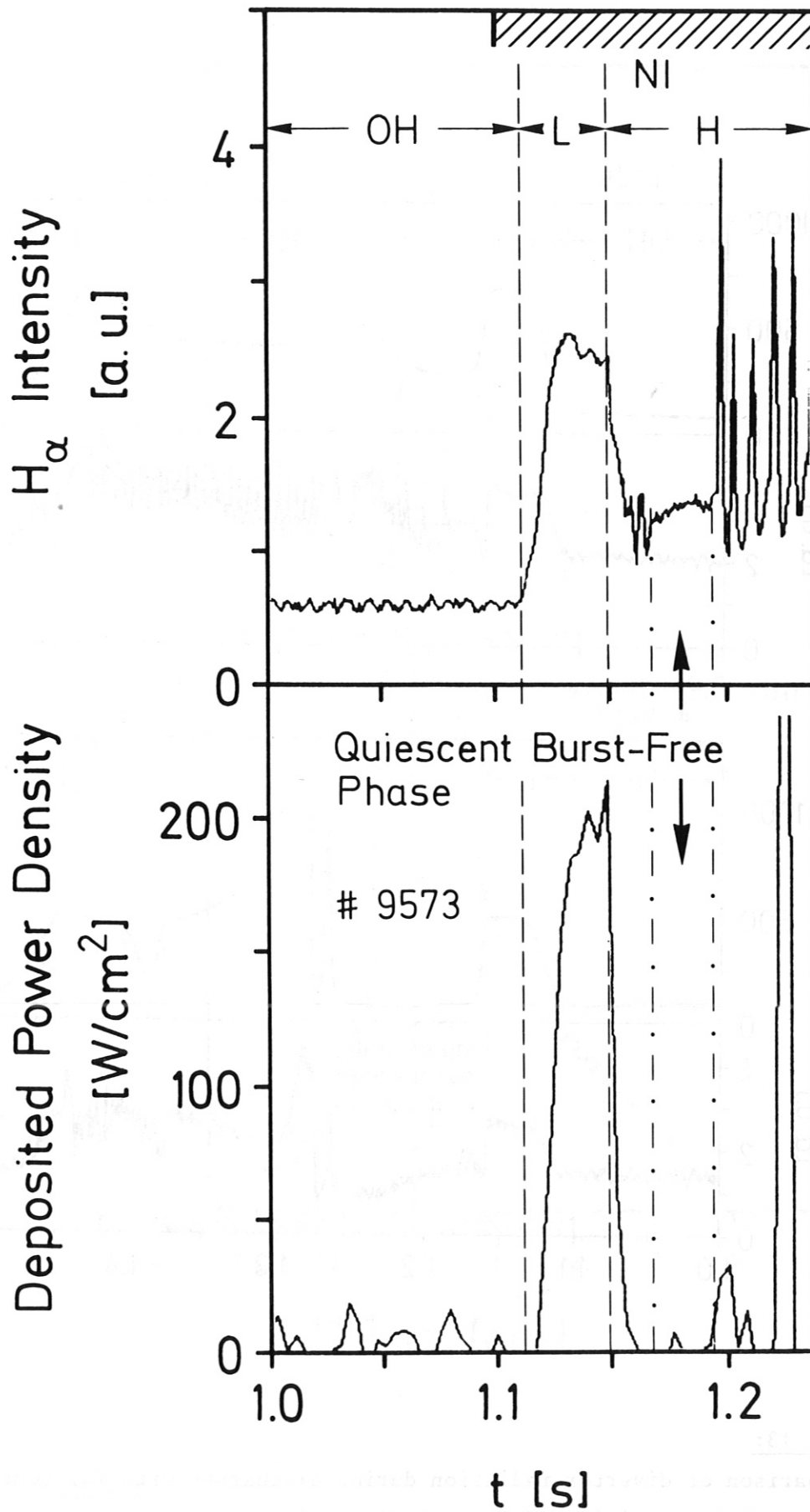


Fig. 12:

$H_\alpha$ -light intensity and deposited power density during the quiescent burst-free H-phase (NB = 3.2 MW,  $I_p = 380$  kA,  $\bar{n}_e = 3.8 \times 10^{13} \text{ cm}^{-3}$ ).

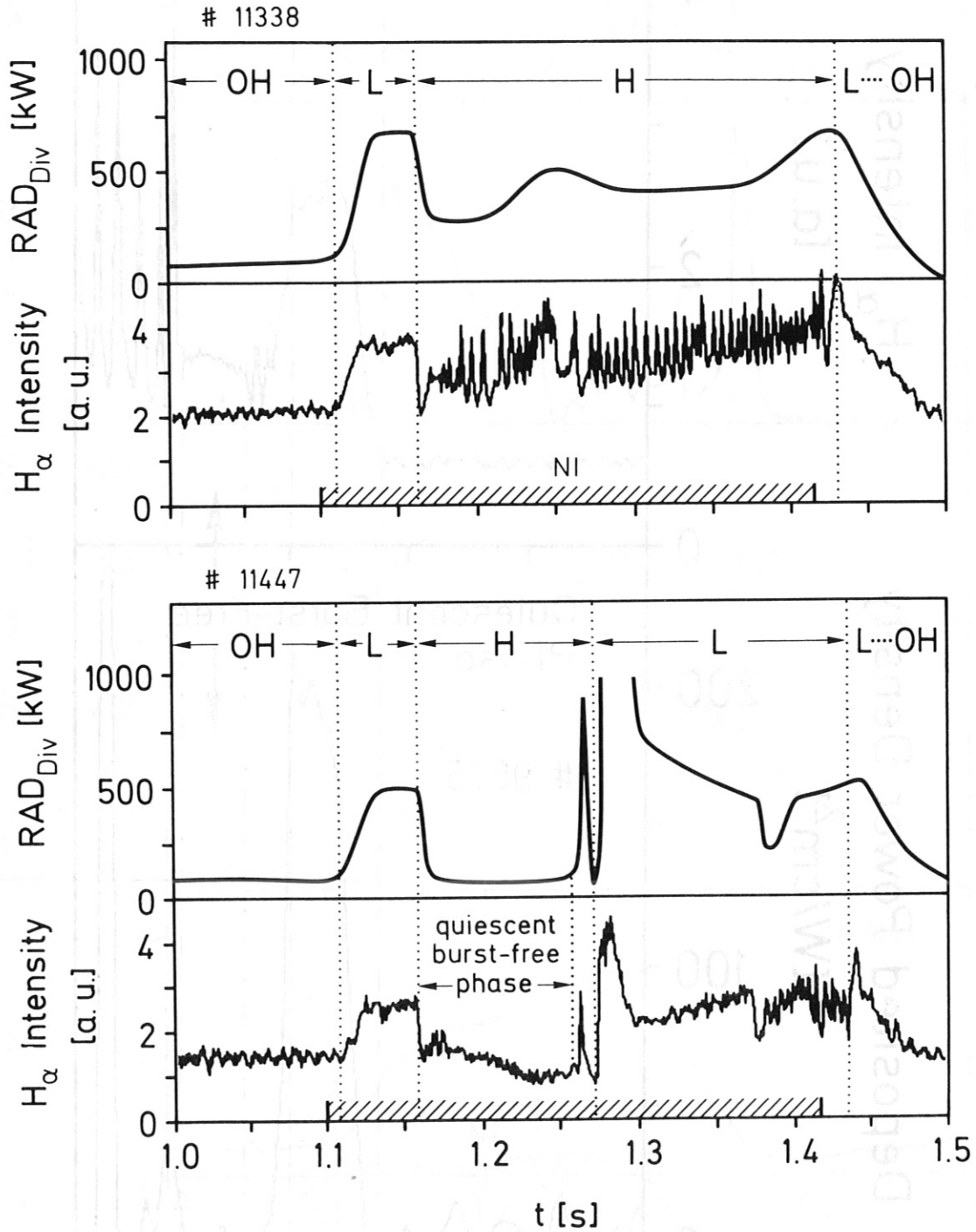


Fig. 13:

Comparison of divertor radiation during discharges with (a) continuous strong burst activity, (b) a relatively long quiescent burst-free H-phase ( $N_B = 3.2$  MW,  $I_p = 320$  kA,  $\bar{n}_e = 3.5 \times 10^{13} \text{ cm}^{-3}$ ).



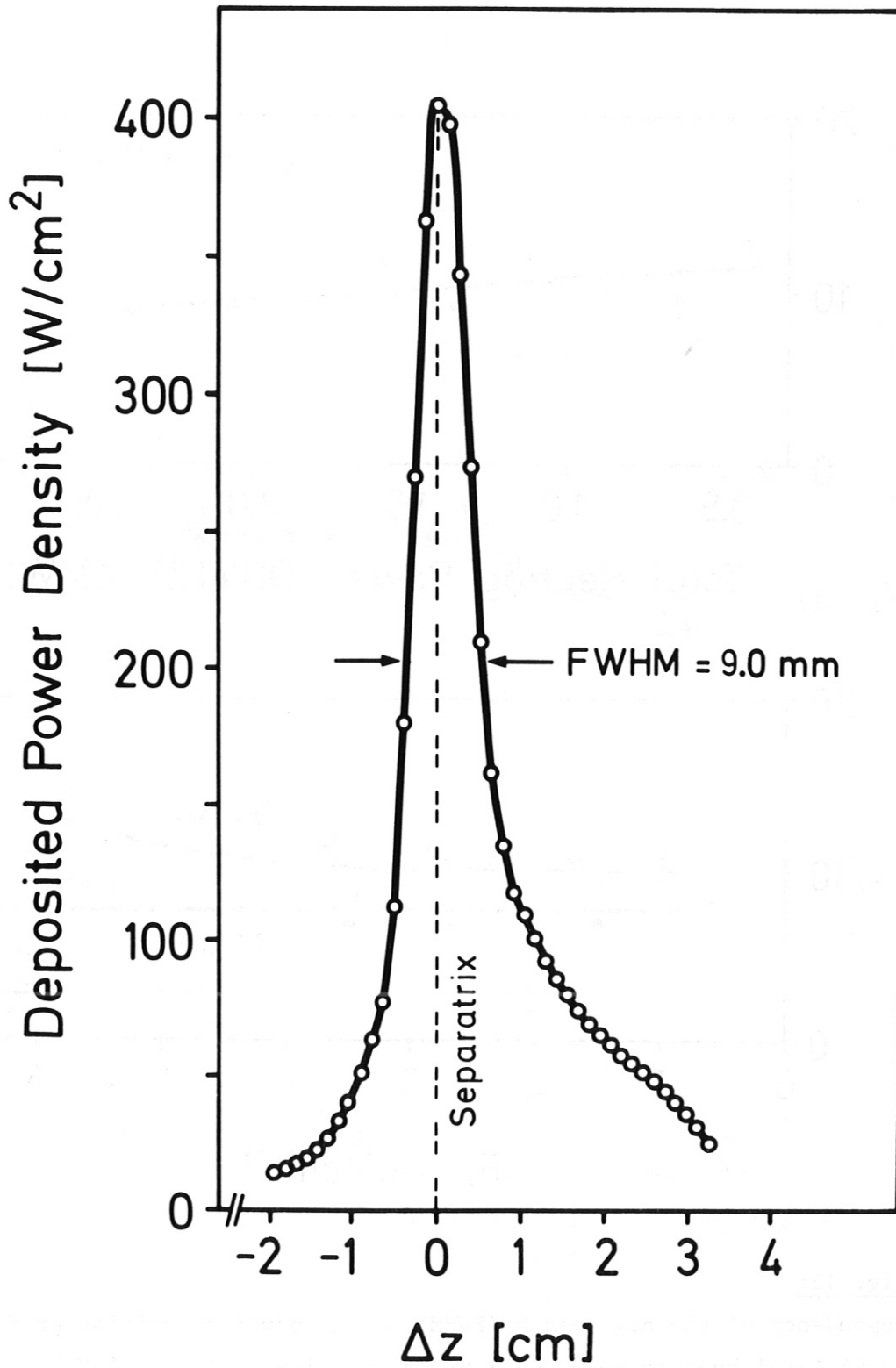


Fig. 14:

Power deposition profile along the poloidal direction of the neutralizer plate during the stationary phase of a neutral-beam-heated discharge in the L-mode ( $I_p = 400$  kA,  $\bar{n}_e = 2.8 \times 10^{13} \text{ cm}^{-3}$ , OH + NB = 2.1 MW).

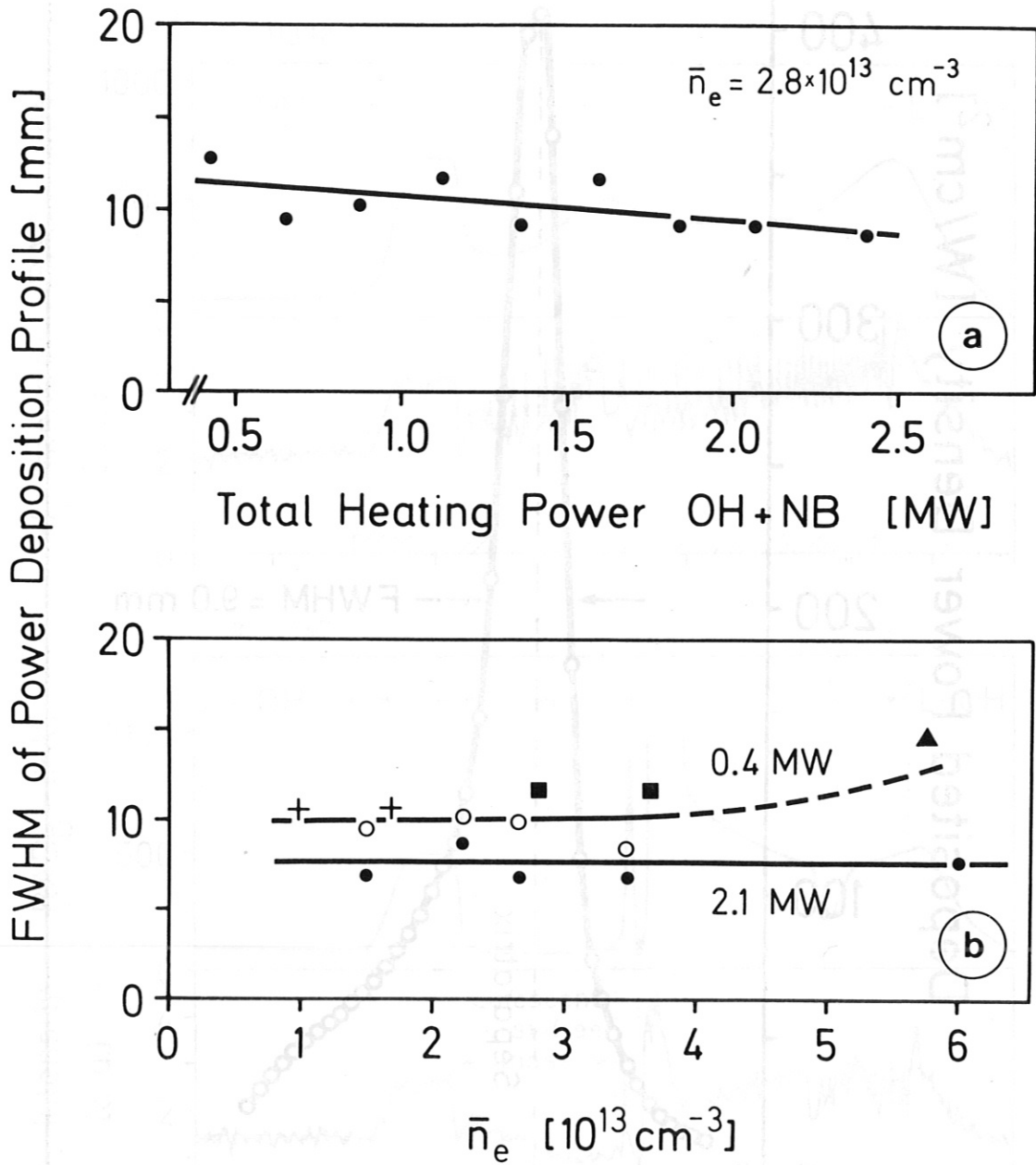


Fig. 15:

Dependence of the half-width (FWHM) of the power deposition profile on a) total heating power OH + NB, b) density  $\bar{n}_e$  (OH: 0.4 MW; NB: 2.1 MW. Different symbols denote different currents  $I_p = 250$  to 400 kA).

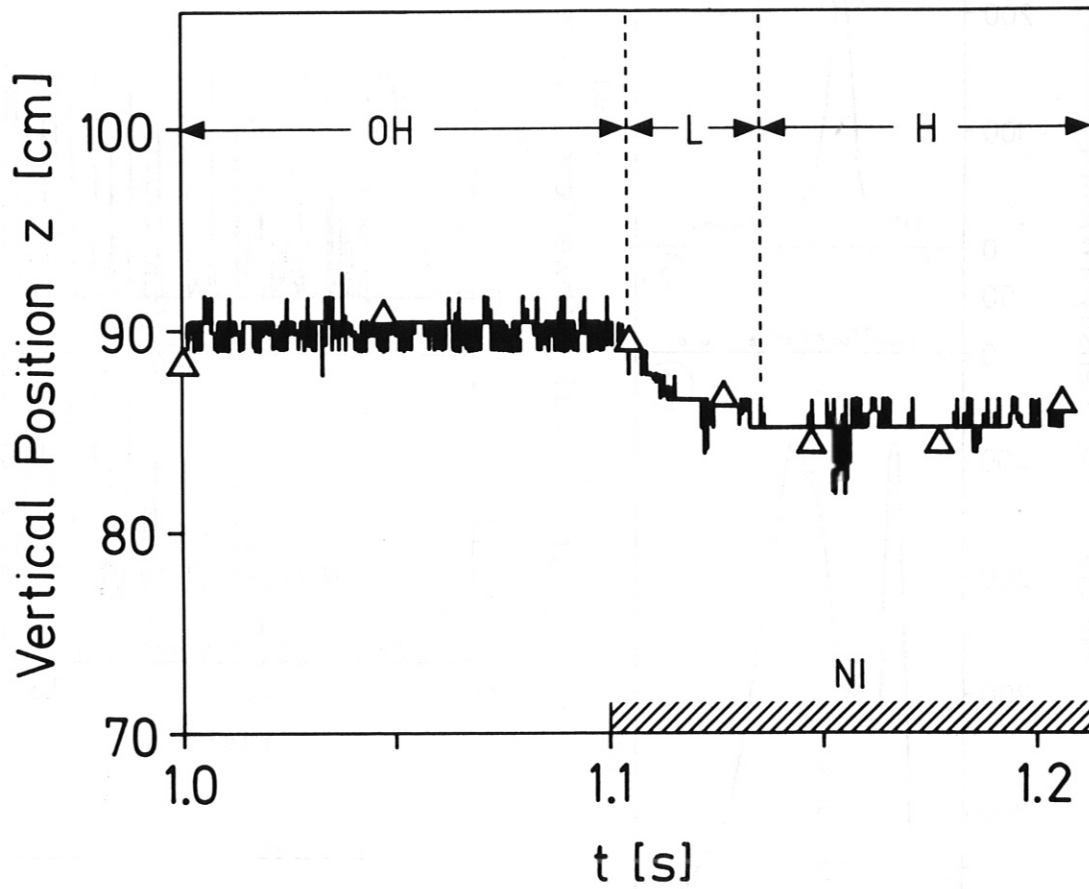
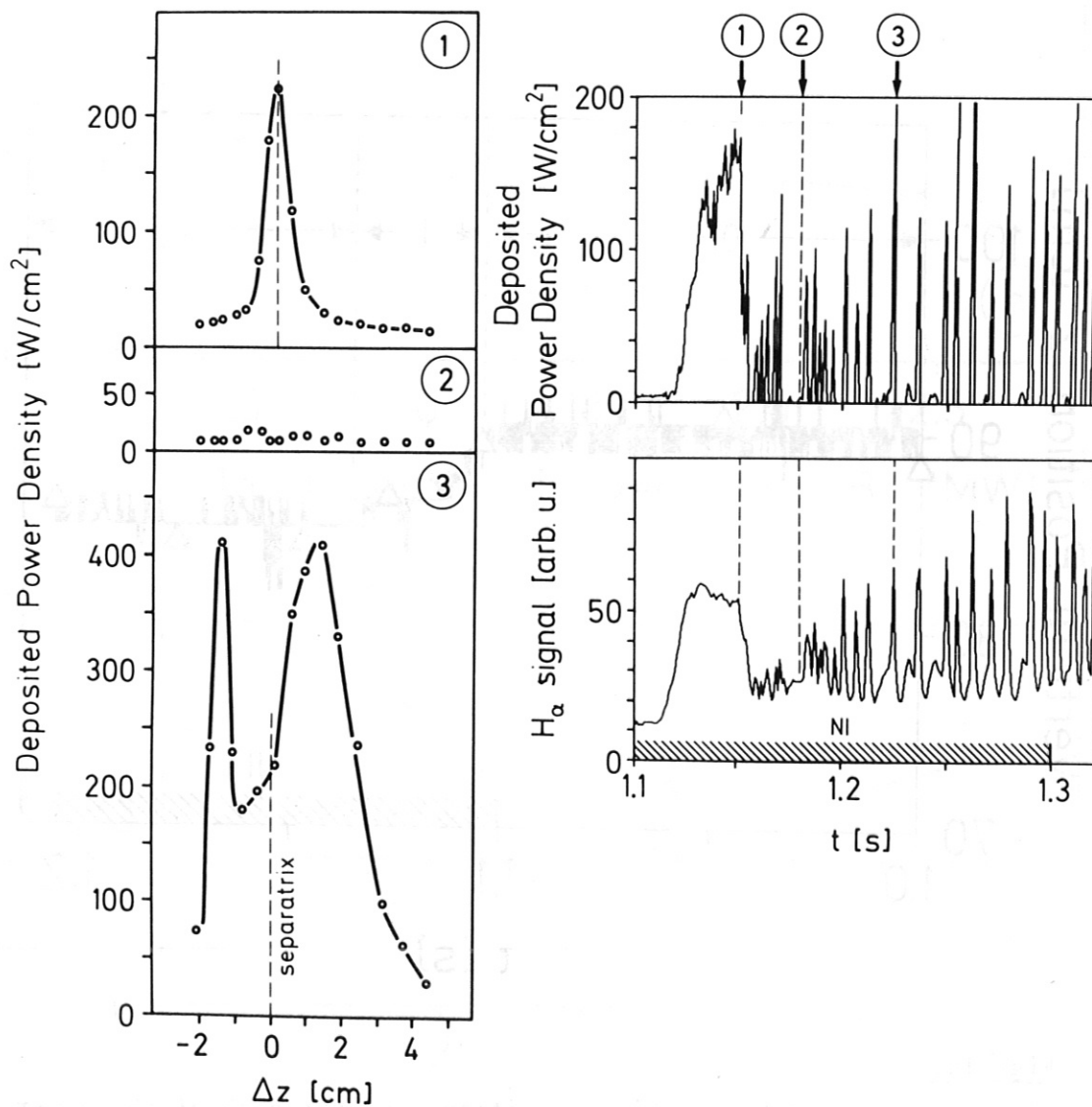


Fig. 16:

Time evolution of the vertical position  $z$  of the peak of the power deposition profile on the neutralizer plates. The triangles represent the separatrix position calculated from magnetic loop signals (NB = 2.8 MW,  $I_p = 320$  kA,  $\bar{n}_e = 3.9 \times 10^{13} \text{ cm}^{-3}$ ).



**Fig. 17:**

Power deposition profiles along the poloidal direction of the neutralizer plate during different neutral-injection phases:

(1) L-phase; (2) quiescent H-phase between bursts; (3) at burst maximum.

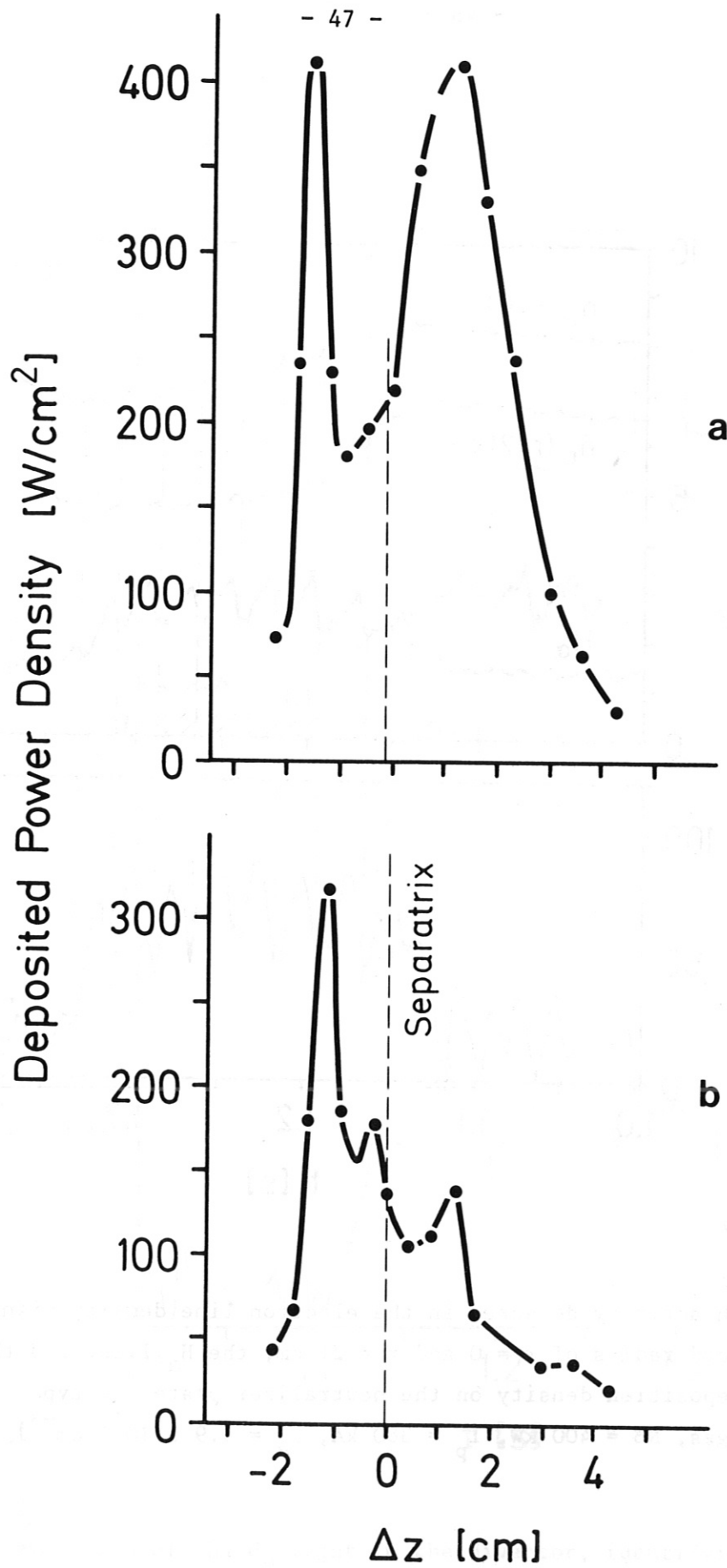


Fig. 18: Power deposition profiles on the neutralizer plates belonging to two different ELMs of the same H-phase (NB = 2.8 MW,  $I_p = 320$  kA,  $\bar{n}_e = 4 \times 10^{13} \text{ cm}^{-3}$ ).



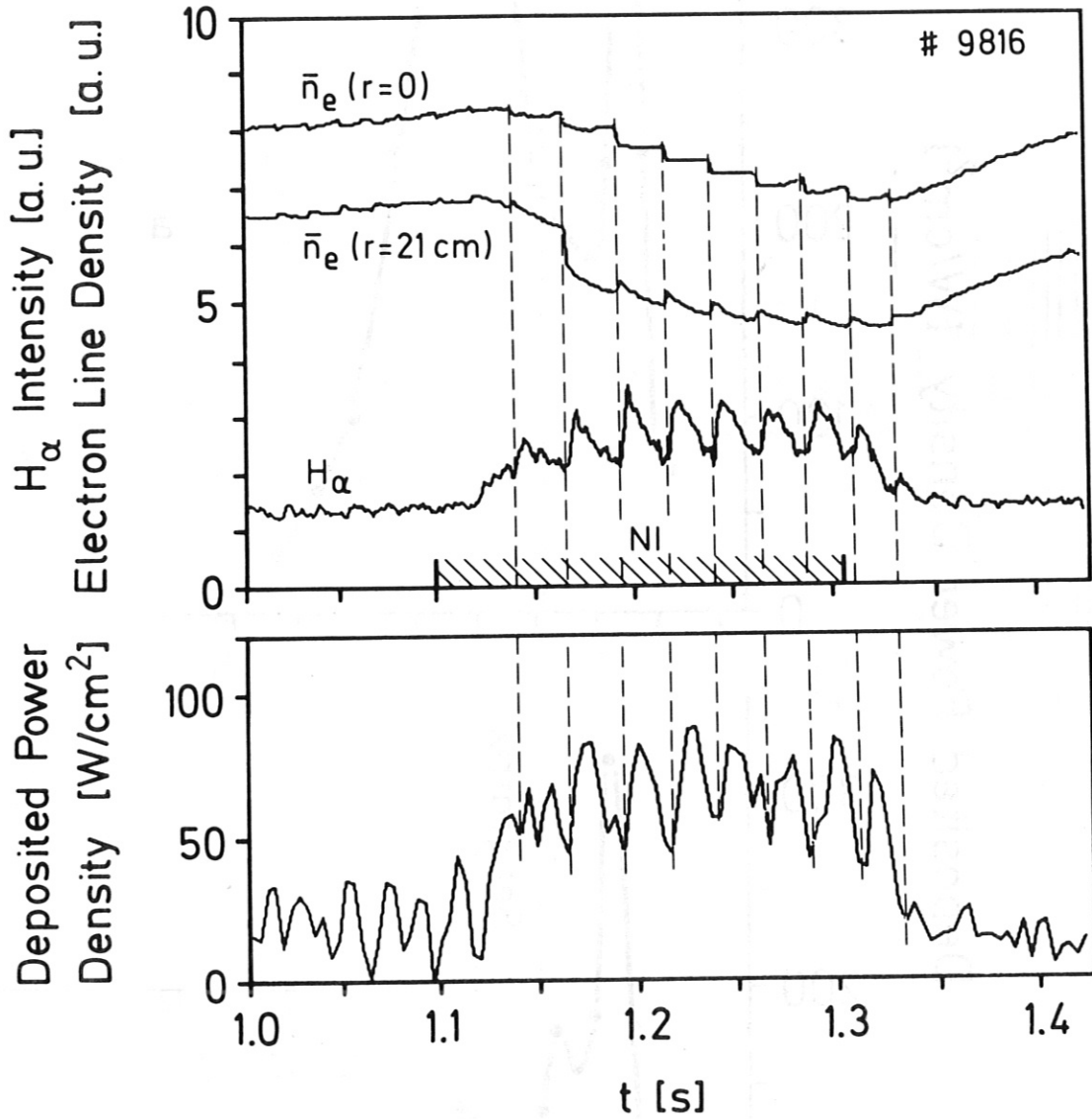


Fig. 19:

Sawtooth activity detected in the electron line density signal at a chord radius of  $r = 0$  and  $r = 21$  cm, the  $H_\alpha$  light and the power deposition density on the neutralizer plates (L-type discharges, NB = 400 kW,  $I_p = 380$  kA,  $\bar{n}_e = 3.9 \times 10^{13} \text{ cm}^{-3}$ ).

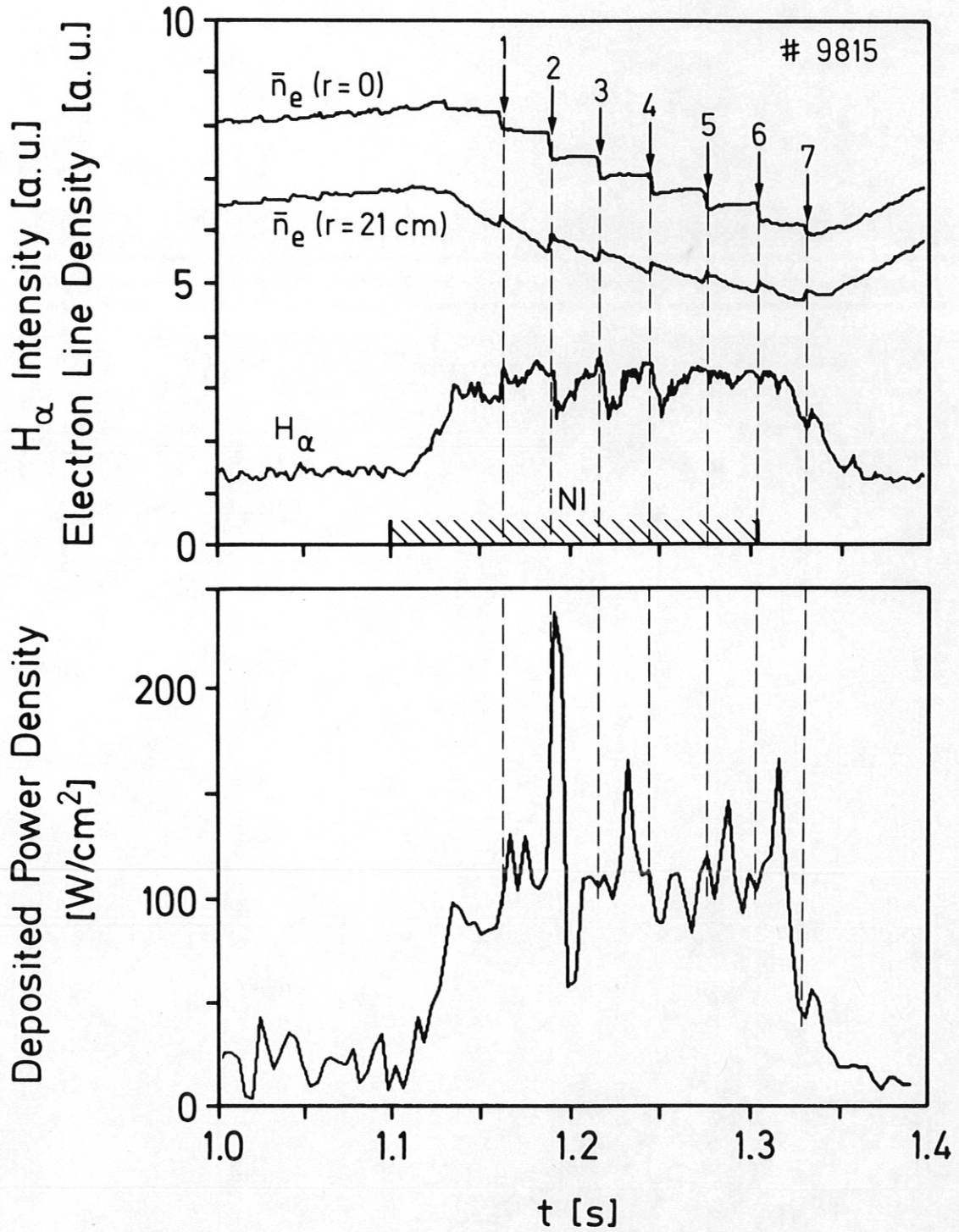


Fig. 20:

Time evolution of the  $H_\alpha$  light in the divertor, identifying short H-phases, and its correlation to the electron line density at a chordal distance of  $r = 0$  and  $r = 21$  cm and to the power deposition density on the neutralizer plates (NB = 800 kW,  $I_p = 380$  kA,  $\bar{n}_e = 3.8 \times 10^{13} \text{ cm}^{-3}$ ).